AD-A266 193

PL-TR-93-2085

NORSAR BASIC SEISMOLOGICAL RESEARCH

Svein Mykkeltveit

NTNF/NORSAR
Post Box 51
N-2007 Kjeller, NORWAY

DTIC
ELECTE
JUN 16 1993
S A D

29 November 1992

Final Report
1 October 1991 – 30 September 1992

93-13532

93 6 15 223

PHILLIPS LABORATORY
Directorate of Geophysics
AIR FORCE MATERIEL COMMAND
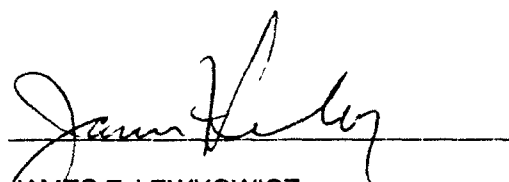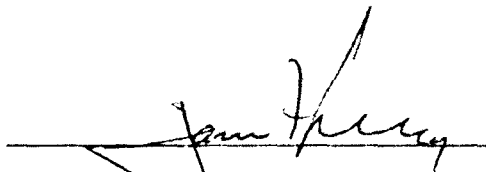**HANSCOM AIR FORCE BASE, MA 01731-3010**

DISCLAIMER NOTICE
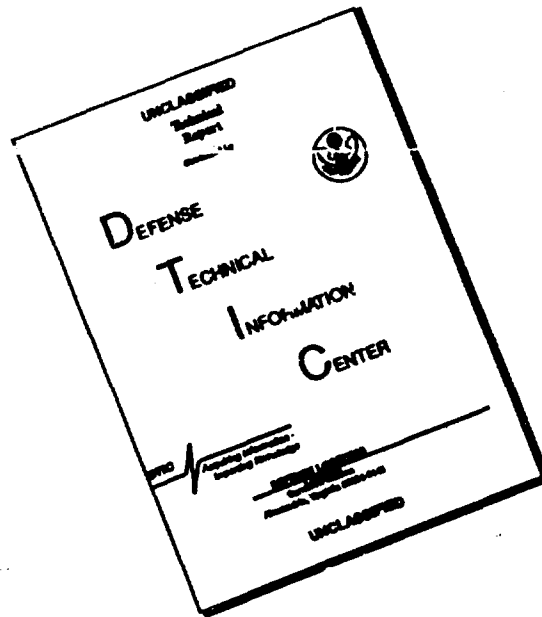
THIS DOCUMENT IS BEST QUALITY AVAILABLE. THE COPY FURNISHED TO DTIC CONTAINED A SIGNIFICANT NUMBER OF PAGES WHICH DO NOT REPRODUCE LEGIBLY.

The views and conclusions contained in this document are those of the authors and should not be interpreted as representing the official policies, either expressed or implied, of the Air Force or the U.S. Government.
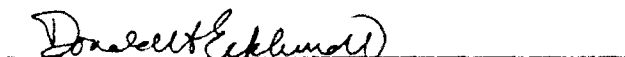
This technical report has been reviewed and is approved for publication.

JAMES F. LEWKOWICZ
Contract Manager
Solid Earth Geophysics Branch
Earth Sciences Division

JAMES F. LEWKOWICZ
Branch Chief
Solid Earth Geophysics Branch
Earth Sciencs Division

DONALD H. ECKHARDT, Director
Earth Sciences Division

REPORT DOCUMENTATION PAGE

Public reporting burden for this collection of information is estimated to average 1 hour per response, including the time for reviewing instructions, searching existing data sources, gathering and maintaining the data needed, and completing and reviewing the collection of information. Send comments regarding this burden estimate or any other aspect of this collection of information, including suggestions for reducing this burden, to Washington Headquarters Services, Directorate for Information Operations and Reports, 1215 Jefferson Davis Highway, Suite 1204, Arlington, VA 22202-4302, and to the Office of Management and Budget, Paperwork Reduction Project (0704-0188), Washington, DC 20503.

1. AGENCY USE ONLY (Leave blank)	2. REPORT DATE	3. REPORT TYPE AND DATES COVERED
	29 November 1992	Final (1 October 1991–30 Sep 1992)

4. TITLE AND SUBTITLE	5. FUNDING NUMBERS
NORSAR Basic Seismological Research	PE 62714E
	PR 9A10 TA DA WU BH
6. AUTHOR(S)	Contract F49620-89-C-0038
Svein Mykkeltveit (Ed)	

7. PERFORMING ORGANIZATION NAME(S) AND ADDRESS(ES)	8. PERFORMING ORGANIZATION REPORT NUMBER
NTNF/NORSAR Post Box 51 N-2007 Kjeller, Norway	

9. SPONSORING/MONITORING AGENCY NAME(S) AND ADDRESS(ES)	10. SPONSORING MONITORING AGENCY REPORT NUMBER
Phillips Laboratory 29 Randolph Road Hanscom AFB, MA 01731-3010 Contract Manager: James Lewkowicz/GPEH	PL-TR-93-2075

11. SUPPLEMENTARY NOTES

12a. DISTRIBUTION/AVAILABILITY STATEMENT	12b. DISTRIBUTION CODE
Approved for public release; distribution unlimited	

13. ABSTRACT (Maximum 200 words)

This Final Report describes the work accomplished under Contract No. F49620-C-89-0038 during the final year of the contract. The report contains 4 separate contributions (paragraphs 2.1 through 2.4), as well as abstracts of the investigations submitted as quarterly technical reports during FY92 (paragraph 2.5).

A systematic analysis of teleseismic P-wave travel time and amplitude variations across the NORSAR array described in paragraph 2.1 reveals that (i) SP time and amplitude anomalies are related, (ii) SP and LP time variations are only partly related, and (iii) LP amplitude variations are very small. The common portion of the SP and LP time residuals can be explained by large-scale structures like a dipping Moho. The frequency dependence of the variations, as well as the relation between SP time and amplitude anomalies, indicates the significance of wavefield diffraction by subsurface structures. When mapping these structures it is thus appropriate to take diffraction into account. This is true even

14. SUBJECT TERMS		15. NUMBER OF PAGES
Time and amplitude variations Later arrivals Detectability	Network expansion Wave propagation Complex media Regional arrays	54
		16. PRICE CODE

17. SECURITY CLASSIFICATION OF REPORT	18. SECURITY CLASSIFICATION OF THIS PAGE	19. SECURITY CLASSIFICATION OF ABSTRACT	20. LIMITATION OF ABSTRACT
Unclassified	Unclassified	Unclassified	SAR

when only travel time data are used, as in seismic tomography, because diffraction effects, including focusing and defocusing, may influence the measurement of phase arrivals and the correlation between signals in an array.

It is generally appreciated that later arrivals contain important information about the seismic source and about the earth's structure. The arrival times of later phases reported to the ISC have been used for tomographic studies of the earth's deep interior, by several workers. However, the quality of these ISC data (as well as other data) has not been properly assessed. For example, it is clear that the data set is incomplete due to missing detections, but it is not clear whether and in which way this will bias inferences from these data. It is expected that the statistics of later arrivals depend not only on the type of phase but also on the performance of the stations reporting this phase. As a first step to evaluate these aspects, bulletin data produced by the large arrays LASA and NORSAR have been analyzed; these arrays can be considered representative of high-quality stations. The phases PcP and PKKP were analyzed, as the detections of these phases were sufficiently numerous to produce meaningful statistics. The results of the investigation are given in paragraph 2.2.

Synthetic seismograms may provide a better understanding of wave propagation in complex media. A novel scheme for computing 2D synthetics based on numerical solutions of the elastic wave equation using finite-difference techniques has been presented in a previous contribution. Recently this scheme has been generalized to models with free surface tomography, and in paragraph 2.3, the usefulness of synthetic seismogram analysis to elucidate wave propagation in the crust and mantle lithosphere is demonstrated. Synthetics are computed for models with increasing structural complexities using a laterally homogeneous lithosphere model as a refrence. The results are displayed in the form of synthetic seismograms, as well as snapshots at 20 sec lapse time. The most important result of these exercises is that the synthetics share dominant wavefield characteristics with seismograms stemming from real recordings of local events, even for relatively simple models of the lithosphere. For example, for many models, the coda excitation relative to the amplitudes of major P- and S-phases is roughly similar to that in real recordings. A practical consequence is that caution should be exercised in reporting weak secondary phases.

Paragraph 2.4 summarizes the status of development of the Northern Europe Regional Array Network. During the fall of 1992, two new small-aperture arrays were added to this network. The new arrays are located near Apatity on the Kola Peninsula of Russia, and on the Arctic island of Spitsbergen. Data from these two new array facilities are now being integrated into the Intelligent Monitoring System, for processing jointly with data from the NORESS, ARCESS, FINESA and GERESS arrays.

Table of Contents

Preface

Under contract No. F49620-C-89-0038, NTNF/NORSAR has been conducting research within a wide range of subjects relevant to seismic monitoring. The emphasis of the research program has been on developing and assessing methods for processing of data recorded by networks of small-aperture arrays and 3-component stations, for events both at regional and teleseismic distances. In addition, more general seismological research topics have been addressed.

This Scientific Report No. 15 is the final report for this four-year effort. It contains four separate contributions relating to research performed during the final year of the contract as well as abstracts for the investigations submitted as quarterly technical reports during FY92.

NORSAR Contribution No. 482

1   Summary

This Final Report describes the work accomplished under Contract No. F49620-C-89-0038 during the final year of the contract. The report contains 4 separate contributions (paragraphs 2.1 through 2.4), as well as abstracts of the investigations submitted as quarterly technical reports during FY92 (paragraph 2.5).

A systematic analysis of teleseismic P-wave travel time and amplitude variations across the NORSAR array described in paragraph 2.1 reveals that (i) SP time and amplitude anomalies are related, (ii) SP and LP time variations are only partly related, and (iii) LP amplitude variations are very small. The common portion of the SP and LP time residuals can be explained by large-scale structures like a dipping Moho. The frequency dependence of the variations, as well as the relation between SP time and amplitude anomalies, indicates the significance of wavefield diffraction by subsurface structures. When mapping these structures it is thus appropriate to take diffraction into account. This is true even when only travel time data are used, as in seismic tomography, because diffraction effects, including focusing and defocusing, may influence the measurement of phase arrivals and the correlation between signals in an array.

It is generally appreciated that later arrivals contain important information about the seismic source and about the earth's structure. The arrival times of later phases reported to the ISC have been used for tomographic studies of the earth's deep interior, by several workers. However, the quality of these ISC data (as well as other data) has not been properly assessed. For example, it is clear that the data set is incomplete due to missing detections, but it is not clear whether and in which way this will bias inferences from these data. It is expected that the statistics of later arrivals depend not only on the type of phase but also on the performance of the stations reporting this phase. As a first step to evaluate these aspects, bulletin data produced by the large arrays LASA and NORSAR have been analyzed; these arrays can be considered representative of high-quality stations. The phases PcP and PKKP were analyzed, as the detections of these phases were sufficiently numerous to produce meaningful statistics. The results of the investigation are given in paragraph 2.2

Synthetic seismograms may provide a better understanding of wave propagation in complex media. A novel scheme for computing 2D synthetics based on numerical solutions of the elastic wave equation using finite-difference techniques has been presented in a previous contribution. Recently this scheme has been generalized to models with free surface tomography, and in paragraph 2.3, the usefulness of synthetic seismogram analysis to elucidate wave propagation in the crust and mantle lithosphere is demonstrated. Synthetics are computed for models with increasing structural complexities using a laterally homogeneous lithosphere model as a refrence. The results are displayed in the form of synthetic seismograms, as well as snapshots at 20 sec lapse time. The most important result of these exercises is that the synthetics share dominant wavefield characteristics with seismograms stemming from real recordings of local events, even for relatively simple models of the lithosphere. For example, for many models, the coda excitation relative to the amplitudes of major P- and S-phases is roughly similar to that in real recordings. A practical consequence is that caution should be exercised in reporting weak secondary phases.

Paragraph 2.4 summarizes the status of development of the Northern Europe Regional Array Network. During the fall of 1992, two new small-aperture arrays were added to this network. The new arrays are located near Apatity on the Kola Peninsula of Russia, and on the Arctic island of Spitsbergen. Data from these two new array facilities are now being integrated into the Intelligent Monitoring System, for processing jointly with data from the NORESS, ARCESS, FINESA and GERESS arrays.

2 Summary of Technical Findings and Accomplishments

2.1 Relation between time and amplitude variations at the NORSAR array

Introduction

The pattern of travel time residuals across the NORSAR array has been studied extensively in the past, with the aim to improve the process of locating teleseismic events. For this purpose Berteussen (1974) constructed a time correction table from SP P-wave residuals at the 22 subarrays for 94 different incident wave directions. The residuals are defined, as is common, as the difference between observed (detected) and theoretical (model) arrival or waveform delay times. Later this correction table was also used to determine the 3D velocity structure beneath NORSAR by seismic tomography (e.g., Aki et al, 1977). It is well known that the SP data also exhibit strong amplitude variations across the array. A relation between time and amplitude variations may be expected on physical grounds and would be diagnostic of the type of 3D subsurface structure, but such a relation has not been experimentally determined. Here we will describe experimental results of reanalyzing the time and amplitude variations at NORSAR.

The data

The waveforms from 86 events of Berteussen's (1974) data set could be retrieved from the data base at NORSAR. The remainder of the events used by Berteussen was either no longer retained at NORSAR, or the signal-to-noise ratio was considered unacceptably low, or the epicentral distances were less than 30°. We omitted these short distances in order to avoid that our results are influenced unduly by the (400 and 650 km) upper mantle discontinuities. We then added the data from 29 other events which were selected so a to achieve the best possible coverage of the incident wave directions. The coverage of our final SP data set is not significantly different from that of Berteussen (1974). We also extracted LP data but only 31 of the 115 events of our SP data set had useful LP waveforms, due to reduced signal-to-noise ratio. Fig. 2.1.1 displays the SP and LP slowness solutions, which can be considered a measure of the incident wave directions. In order to list methods of measuring travel time residuals, and to get a detailed view of the pattern of both time and amplitude anomalies, we acquired an additional data set from a cluster of events in the Kurile Islands, at 70° distance from the array. We selected SP data from 19 events, and LP data from 6.

For the purpose of measuring travel time residuals, we found that an iterative method of cross-correlating subarray beam waveforms with the array beam, a method similar to the one originally used at NORSAR, works well for the SP data, but the LP results were obtained by replacing cross-correlation by least-squares waveform fitting, allowing both the time lag and the amplitude of the waveforms to vary. Our procedure of waveform fitting minimizes the difference between subarray and array beams. The data windows used in these methods were about 1.5 times the dominant signa period, i.e., 1.5 s for SP data

and 30 s for LP data. Note that these methods produce residuals relative to the array beam, which can be regarded as an average over the array.

Time and amplitude variations

Fig. 2.1.2 shows the time and amplitude variations across the array, of SP and LP P waves from he Kurile Islands events. We did not plot the LP amplitude variations as these were very small. Fig. 2.1.2 illustrates well the large SP anomalies in both time (~1 s) and amplitude (~ factor 10). The pattern of variations suggests that early arrivals tend to have small amplitudes, whereas the amplitudes of the later arrivals are less consistent. The LP time residuals also show a systematic pattern, which is however different from the SP pattern; the early arrivals in particular are less pronounced. Similar characteristics can be inferred from the data for all events. It is customary to express the variation of time residuals across an array or network by means of the variance σ^2. On average, σ^2 is about 0.044 s^2 for the SP time residuals, and about 0.029 s^2 for the LP time residuals.

Fig. 2.1.3 shows the SP and LP residuals averaged over all events, for each of the 22 sub-arrays. There is a clear east-to-west trend in both the SP and LP time residuals, with early arrivals to the east and late arrivals to the west. This may be explained by a dipping Moho, which is consistent with independent evidence of such a structure. Another prominent feature is the pattern of large SP amplitudes in the northeast, which has no obvious counterpart in the time residuals. This amplitude pattern was recognized earlier and in fact played a major role in the site selection of the NORESS array (Mykkeltveit et al, 1990).

The relation between SP time and amplitude anomalies is shown in Fig. 2.1.4. Fig. 2.1.4a is the usual scatter diagram. In Fig. 2.1.4b the time residuals are binned and the amplitude anomalies are averaged as a function of time residual. In Fig. 2.1.4c the amplitude residuals are binned and the time residuals are averaged as a function of amplitude anomaly. The pattern is in agreement with the results for one source region plotted in Fig. 2.1.2: There is a clear relation between early arrivals and small amplitudes. High-amplitude arrivals tend to be late (Fig. 2.1.4c), but late arrivals do not necessarily have high amplitudes (Fig. 2.1.4b). This suggests that, while focusing by low-velocity structures does occur, the focus is not necessarily near the surface. This interpretation is strengthened by the synthetic data for a model of the structure beneath NORSAR (Ødegaard and Doornbos, 1992); the patterns of the synthetics plotted in Fig. 2.1.4 are very similar to the real data.

Conclusions

A systematic analysis of teleseismic P-wave travel time and amplitude variations across the NORSAR array reveals that (i) SP time and amplitude anomalies are related, (ii) SP and LP time variations are only partly related, and (iii) LP amplitude variations are very small. The common portion of the SP and LP time residuals can be explained by large-scale structures like a dipping Moho. The frequency dependence of the variations, as well as the relation between SP time and amplitude anomalies, indicates the significance of wavefield diffraction by subsurface structures. When mapping these structures it is thus appropriate to take diffraction into account. This is true even when only travel time data are used, as in seismic tomography, because diffraction effects, including focusing and

defocusing, may influence the measurement of phase arrivals and the correlation between signals in an array.

E. Ødegaard, Univ. of Oslo
D.J. Doornbos

References:

Aki, K., A. Christoffersson and E.S. Husebye (1977): Determination of the three-dimensional structure of the lithosphere, *J. Geophys. Res.*, 82, 277-296.

Berteussen, K.-A. (1974): NORSAR location calibrations and time delay corrections, NORSAR Sci. Rep. 2-73/74.

Mykkeltveit, S., F. Ringdal, T. Kværna and R.W. Alewine (1990): Application of regional arays in seismic verification research, *Bull. Seism. Soc. Am.*, 80B, 1777-1800.

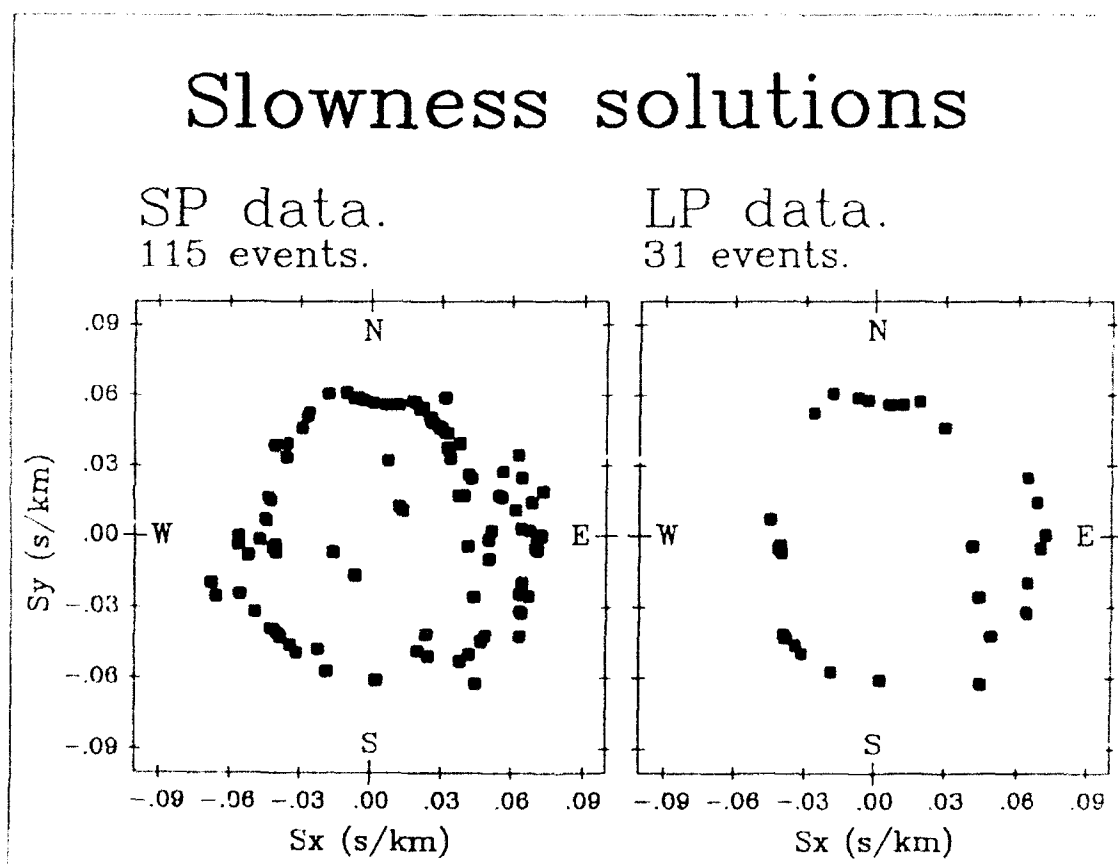Odegaard, E. and D.J. Doornbos (1992): Seismic diffraction tomography of array data, *J. Geophys. Res.*, in press.

Slowness solutions

SP data.
115 events.

LP data.
31 events.

Fig. 2.1.1. Slowness diagram of P-waves. Slowness solutions indicate the direction to the sources.
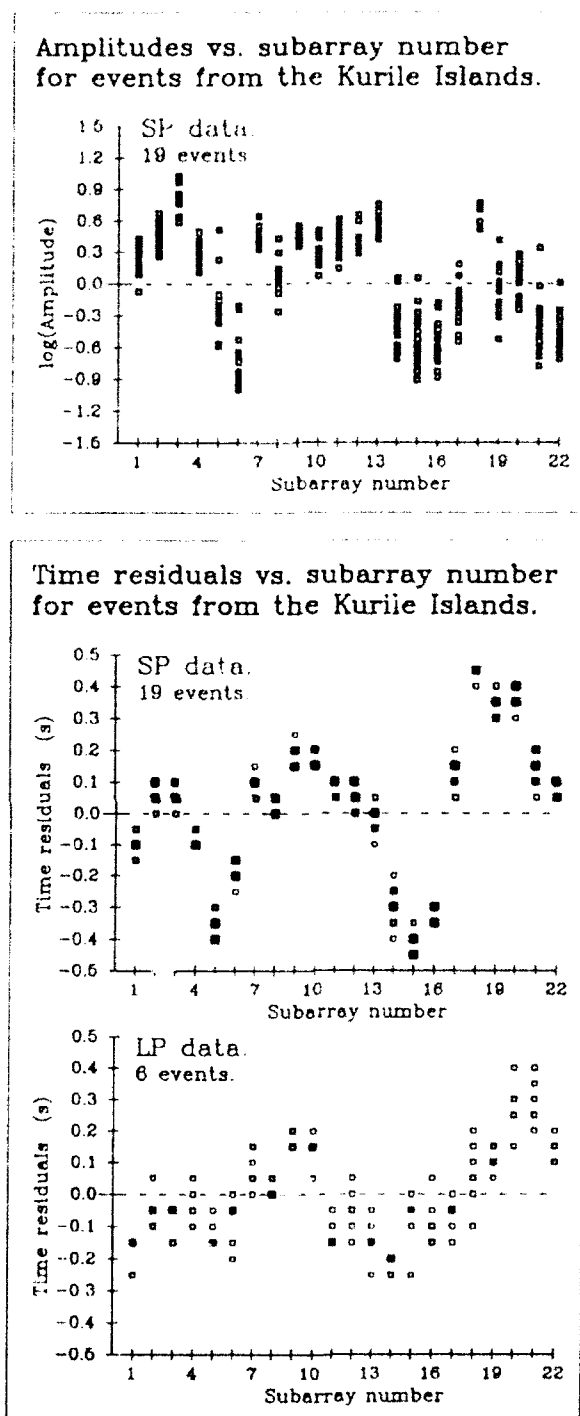
Fig. 2.1.2. SP peak-to-peak amplitude and time residual variation at the 22 subarrays for 19 events, and LP time residual variation for 6 events from Kurile Islands. Peak-to-peak amplitudes are measured relative to the array beams. Symbol size is proportional to amount of data.
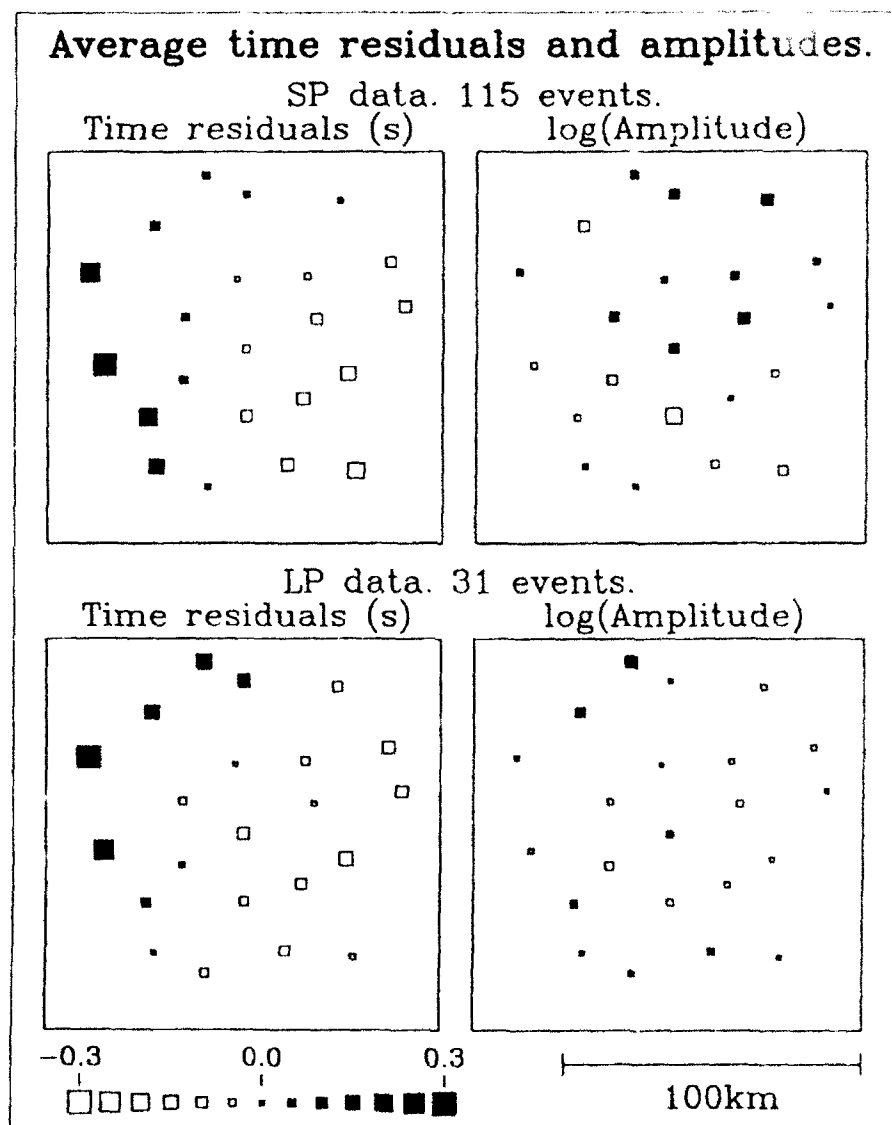
Average time residuals and amplitudes.

SP data. 115 events.

Fig. 2.1.3. Average SP and LP residuals for each of the 22 subarrays. The values are computed by first averaging the residuals within 15 equal azimuth intervals, and then averaging over all azimuth intervals.

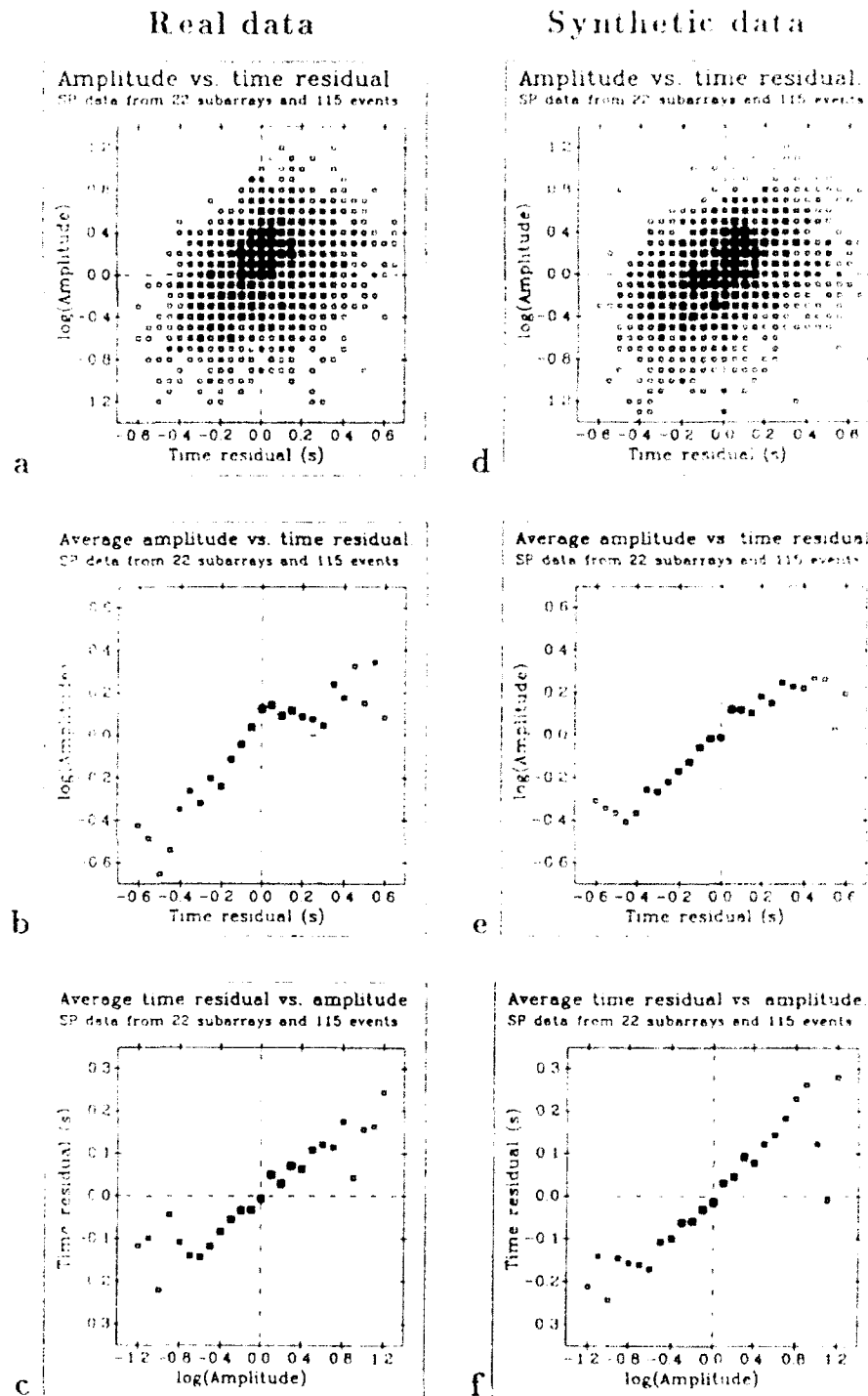Real data   Synthetic data

Fig. 2.1.4. (a) Scatter diagram of observed SP peak-to-peak amplitude residual vs time residual for the 22 subarrays and 115 events; (b) Average peak-to-peak amplitudes residual vs binned time residual for the data plotted in (a); (c) Average time residual vs binned amplitude residual for the data plotted in (a); (d,e,f) Same as (a,b,c) but for synthetic data derived from a model for the velocity structure beneath NORSAR.

2.2   Station performance in detecting later arrivals

Introduction

It is generally appreciated that later arrivals contain important information about the seismic source and about the earth's structure. The arrival times of later phases reported to the ISC have been used for tomographic studies of the earth's deep interior, by several workers (e.g., Doornbos and Hilton, 1989). However, the quality of these ISC data (as well as other data) has not been properly assessed. For example, it is clear that the data set is incomplete due to missing detections, but it is not clear whether and in which way this will bias inferences from these data (e.g., Vinnik and Dashkov, 1970). It is expected that the statistics of later arrivals depend not only on the type of phase but also on the performance of the stations reporting this phase. As a first step to evaluate these aspects, we have analyzed bulletin data produced by the large arrays LASA and NORSAR in the past; these can be considered representative of high-quality stations. We selected time intervals during which a detector was applied consistently, i.e., April 1969 - December 1970 for LASA and April 1971 - August 1976 for NORSAR. We analyzed PcP and PKKP as the detections of these phases were sufficiently numerous to produce meaningful statistics. In this report we are primarily concerned with the statistics of detections and amplitudes, and we have conducted simulation experiments to explain the general characteristics of these data. Travel time data will be presented elsewhere.

Detection characteristics

Fig. 2.2.1 summarizes the performance of LASA in detecting PcP. The results are based on PcP detections for epicentral distances up to 60°. For larger distances there is an increasing number of P coda arrivals that are misidentified as PcP; evidence for this is provided by inspecting the slowness solutions for these arrivals. For each event magnitude, the number of detections was divided by the total number of events in the chosen distance range ($20-60^\circ$). The ratio is plotted as "detection rate", which can vary between 0 and 1. Also plotted is the averaged amplitude for each magnitude. In order to merge the data from different events, magnitudes are adjusted so as to represent surface focus events, and amplitudes are adjusted so as to represent PcP at 40° distance.

The following characteristics are apparent: At low magnitudes, the detection rate drops sharply with decreasing magnitude, whereas amplitude levels off in this range. At higher magnitudes the detection rate levels off (at a rate less than 1) and amplitude increases with magnitude, slightly above the theoretical amplitude for a spherical earth model. The latter result is of course dependent on the actual model used (in particular, on the impedance contrast across the core-mantle boundary); the values shown here are for PREM.

The summary of PKKP detections at LASA (Fig. 2.2.2) displays similar characteristics. The results are based on detections of the BC branch of PKKP in the distance range between 80 and 120°, and the amplitudes are adjusted to a reference distance of 100°. PKKP is an order of magnitude smaller than PcP, hence the PKKP detections occur for larger event magnitudes. The PcP and PKKP detections at NORSAR are consistent with the summary results for LASA, but detections do not extend to the same low magnitudes

as for LASA, and there are less suitable events within 60° from NORSAR and hence less PcP data for this array.

Numerical simulations

Many of the detection characteristics of later phases can be understood as a consequence of signal variations in the presence of noise. Rekdal and Doornbos (1992) simulated the detection process under such circumstances and studied the effect on travel time residuals. We have conducted similar experiments with the primary aim to explain the detection rate and amplitude data (as displayed for PcP and PKKP). Signal variations are produced by passing a seismic pulse through an aspherical structure. The aspherical part of the models considered by Rekdal and Doornbos is confined to a region at or near the core-mantle boundary. Our experiments are based on the same models, although for the present purpose the source of signal variations is immaterial; it is only required that the variations are of the observed order of magnitude. We use a simple detection criterion, and declare a detection when the amplitude of the pulse exceeds a prespecified threshold that depends on the noise level. In order to acquire a statistical basis for our results, we apply the detector to a pulse at one given epicentral distance, for 25 different realizations of the aspherical structure. The differences are generated simply by "phase shifting", i.e., shifting the maxima and minima of the perturbations in structure. For the models considered here, the resulting signal amplitude variations are up to about a factor of 5.

We scale the results in relation to a reference amplitude for the spherical model. In order to present the results in a form comparable to the real data, we introduce a reduced magnitude scale, and (arbitrarily) identify zero magnitude with unit amplitude for the spherical model. Finally we have to specify the noise level or detection threshold on this scale. The examples shown in Figs. 2.2.3 and 2.2.4 are based on a constant detection threshold equal to unit amplitude for the spherical model. Fig. 2.2.3 shows results for PcP at 60° epicentral distance, where the aspherical structure consists of a laterally varying boundary layer at the base of the mantle (model 2 of Rekdal and Doornbos, 1992). Fig. 2.2.4 shows similar results for PKKP at 100° epicentral distance, and the asphericity is here modeled by a laterally varying core-mantle boundary at the point of underside reflection of the phase (model 6 of Rekdal and Doornbos, 1992).

Detection rate and amplitude bias

Figs. 2.2.3 and 2.2.4 illustrate well some of the same characteristics as seen in the real data: Toward low magnitudes the detection rate drops sharply and the amplitude levels off to a value just above the noise level. Toward high magnitudes the detection rate levels off to a constant value and log-amplitude increases in proportion to magnitude. However, two differences with the real data should be noted: (1) The averaged amplitude of the synthetics falls below the amplitude for a spherical model, and (2) the constant detection rate equals 1 (i.e., all phases are detected), in contrast to the real data.

The relatively low amplitude average of the synthetics is probably due to our averaging procedure. We averaged log-amplitudes, which is consistent with the usual assumption that the amplitude distribution is log-normal (e.g., Vinnik and Dashkov, 1970). However,

inspection of the synthetic data reveals that their distribution is not log-normal; it appears that for these data, averaging amplitude squared (as a measure of energy) produces results close to the values for a spherical model.

The difference in detection rate between the synthetics and the real data can be explained by our choice of constant background noise level in the simulations. A reasonable alternative might be to assume that the noise level increases with event magnitude since in the context of detecting later arrivals, "noise" is actually comprised of the coda of P. A limit case is to adopt a model where the logarithm of coda level increases in proportion to magnitude. The detection rate will then go to a constant less than 1, and the accompanying amplitude average will be biased upward. For the purpose of estimating this bias we assume, guided by the real data, a final detection rate of 50%, i.e., log rate = -0.3. For our PcP model this detection level would be reached for a reduced magnitude near 0.15, and the amplitude bias would be about 0.15 log-units (~40%). For the PKKP model, a detection level of 50% would be reached for a reduced magnitude near 0.25, and the associated amplitude bias would be about the same as for PcP, i.e., about 40%. It remains to be investigated how representative these values are for different models of signal variation.

D.J. Doornbos
T. Rekdal, Univ. of Oslo

References

Doornbos, D.J. and T. Hilton (1989): Models of the core-mantle boundary and the travel times of internally reflected core phases, J. Geophys. Res., 94, 15741-15751.

Rekdal, T. and D.J. Doornbos (1992): The times and amplitudes of core phases for a variable core-mantle boundary layer, Geophy. J. Int., 108, 546-556.

Vinnik, L.P. and G.G. Dashkov (1970): PcP waves from atomic explosions and the nature of the core-mantle boundary, Isv. Earth Physics, 1, 7-16.
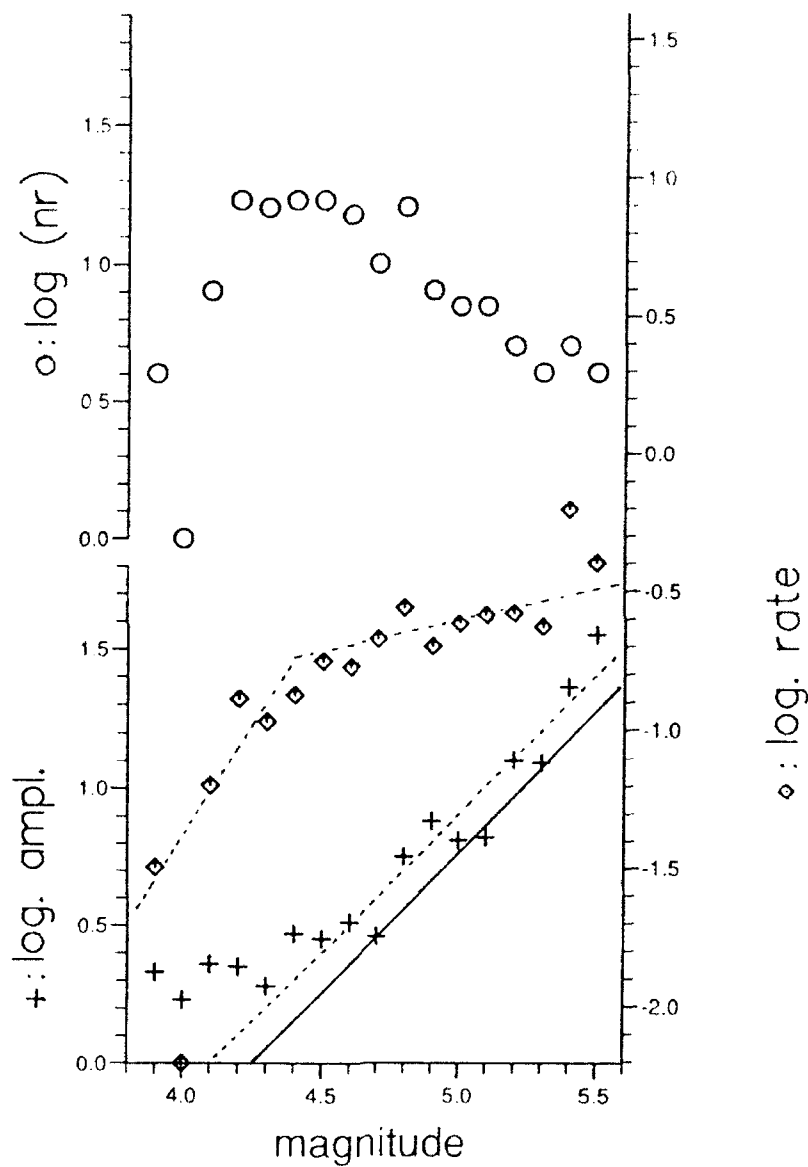
Fig. 2.2.1. Detection and amplitude statistics of PcP at LASA. Epicentral distance range is 20-60°. Number of detections (O), detection rate (◊), and averaged amplitudes in nm (+), as a function of event magnitude. All data in log-units. The dotted lines suggest trends in the data. The solid line represents the PcP amplitude for a spherical model (PREM).
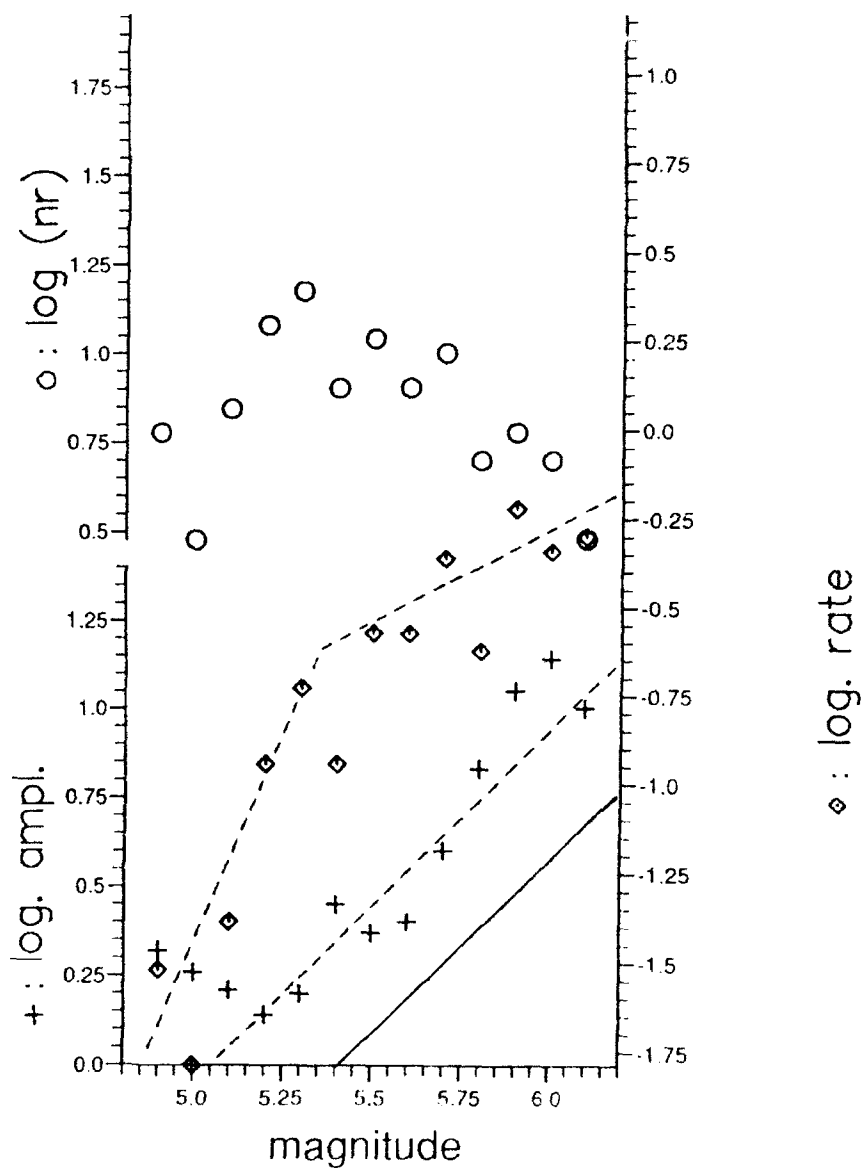
Fig. 2.2.2. Detection and amplitude statistics of PKKP(BC) at LASA. Epicentral distance range is 80-120°. Other details as in Fig. 2.2.1.
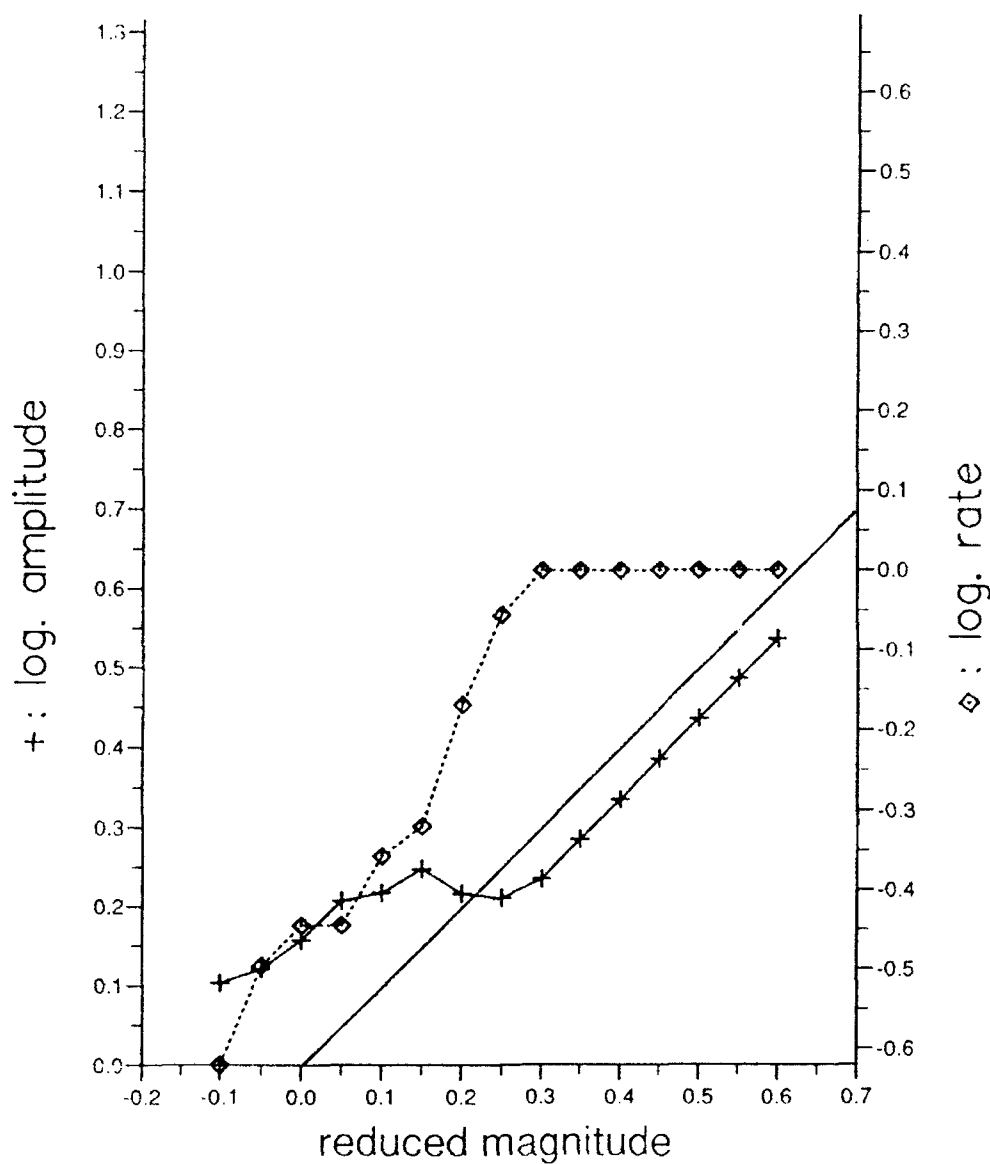
Fig. 2.2.3. Simulation of detection and amplitude statistics of PcP. Signal variations at 60°
epicentral distance generated for model 2 of Rekdal and Doornbos (1992). Detection
rate (◇) and averaged amplitude (+) as a function of reduced magnitude. Magnitude
and PcP amplitude are scaled so that amplitude 1 relates to magnitude 0. The solid
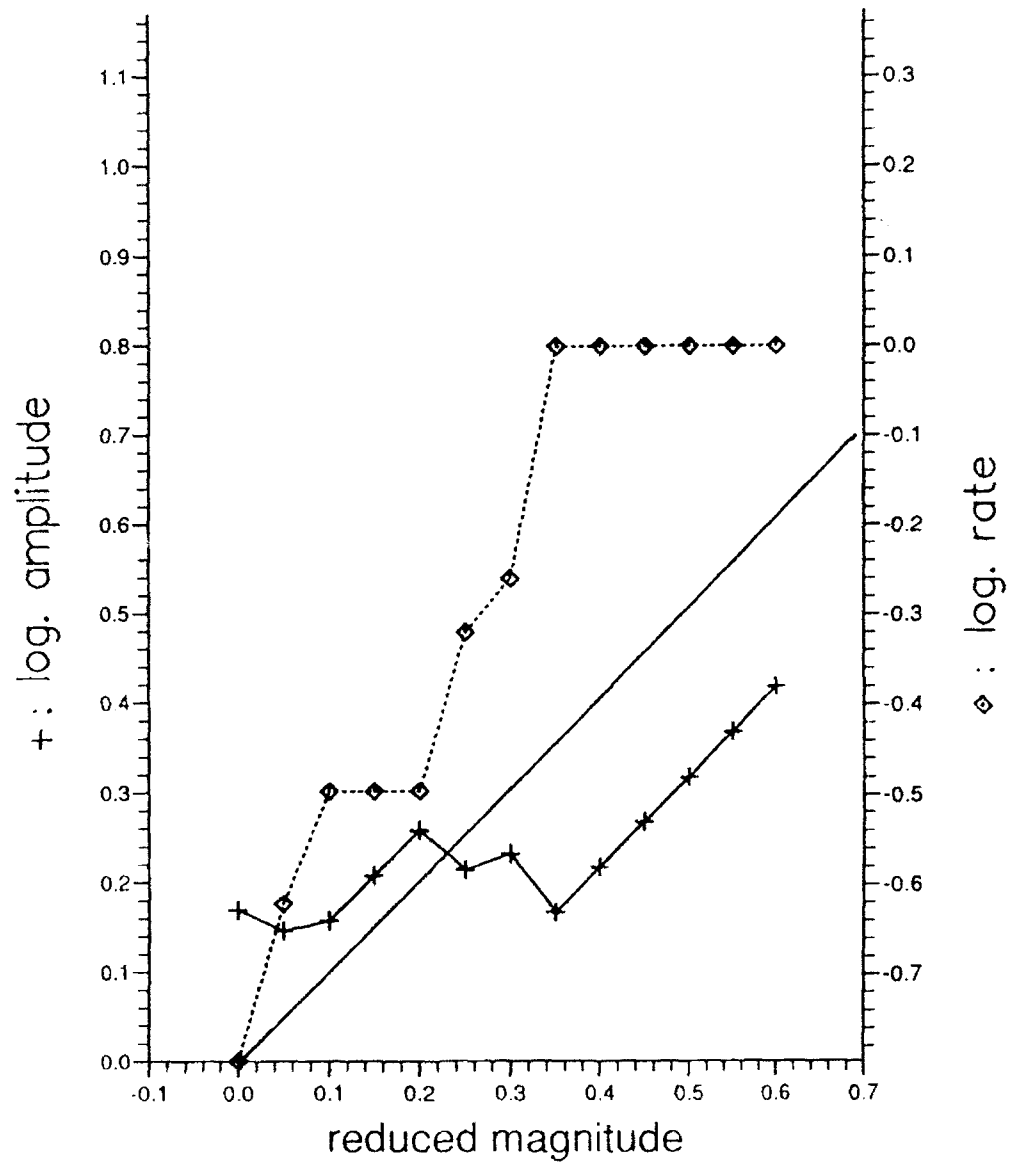line through 0 represents the amplitude for a spherical model (PREM).

Fig. 2.2.4. Simulation of detection and amplitude statistics of PKKP(BC). Signal variations at 100^0 epicentral distance generated for model 6 of Rekdal and Doornbos (1992). Other details as in Fig. 2.2.3.

2.3   Visualizing seismic wave propagation in complex media

Synthetic seismograms may provide a better understanding of wave propagation in complex media. In a previous contribution, we have presented a novel scheme for computing 2D synthetics based on the elastic wave equation. Its numerical solutions are obtained using finite-difference (FD) techniques (Hestholm et al, 1992). Recently, the above scheme has been generalized to models with free surface topography (Hestholm and Ruud, 1993). In this contribution we demonstrate the usefulness of synthetic seismogram analysis to elucidate wave propagation in the crust and mantle lithosphere.

Scattering representation of the lithosphere

Traditionally, the earth is often modelled as a simple stratified medium, each of the layers having constant physical properties. Seismograms from these models tend to match the gross features of observational records but lack the variations in amplitude and travel time and coda waves accompanying major arrivals. These features are symptomatic of scattering from small-scale changes in velocity and/or density that depend on the size, distribution and magnitude of the heterogeneities. For a better understanding of high-frequency (> 1 Hz) seismic wave propagation in the lithosphere structural system, realistic models must include small-scale inhomogeneities. In contrast, the class of ray tracing synthetics for crustal models even with many layers does not contain the coda-scattering wavelets typical of all observational records.

In the literature on seismic wave scattering, heterogeneous media are commonly described in terms of a few physical parameters like thickness of the scattering layer, heterogeneity correlation distance a (in case of spatial anisotropic correlation functions a_x, a_z) and heterogeneity fluctuation (RMS). We may limit fluctuations to either velocity or density and also introduce corrugated layer boundaries. In our models, the preference was for 2D von Kármán inhomogeneous media realizations due to their versatility. For example, with proper choice of the order parameter υ we can generate both exponential and self-similar inhomogeneous media models (Frankel and Clayton, 1986; Toksöz et al, 1988; Charette, 1991) as well as intermediate types. Also, 1D von Kármán realizations proved convenient for generating topography and corrugated Moho interfaces.

The basic model parameters are a crustal thickness of 35 km, and with a constant velocity gradient both above and below the Moho, as illustrated in Fig. 2.3.1. P- and S-velocities are related through the Poisson's ratio of 0.25, and model densities are calculated from the P-velocities via Birch's (1961) law. In our calculations of synthetics, the above basic model has been perturbed in various ways (Table 2.3.1). An example of a model realization is shown in Fig. 2.3.2.

Elucidating wave propagation in a complex lithosphere

From the above model section we have that the number of potential complex lithosphere models are legio. However, to get a proper understanding of the relative contributions from the various parts of the lithosphere to the seismogram we need to isolate these contri-

butions. We have achieved this by computing synthetics for models with increasing structural complexities using a laterally homogeneous lithosphere model as a reference. The synthetics here are depicted in Fig. 2.3.3 for both P- and S-sources (pure divergence and curl sources, respectively, see Hestholm et al (1992) for details), and the seismograms here are rather simila. to those obtained using ray-tracing techniques. The next steps, while retaining large-scale structural features, were to perturb the Moho interface and then to introduce free surface topography. The results here are displayed in the form of synthetic seismograms (Fig. 2.3.4, Moho corrugations) and snapshots at 20 sec (Fig. 2.3.5, topography). Obviously, Moho corrugations do not contribute much towards seismogram complexities, not at least a few kilometers away from this boundary. On the other hand, free surface topography contributes significantly towards coda excitation in terms of efficient P-to-Rg scattering. A non-flat surface will also affect the P-slowness measurements. A smoothed version of the NORESS siting area topography could account for about half of the observed anomalies for this array. Note that topography models (1D von Kármán realizations with order 1.0 and 10 km correlation distance) with RMS exceeding 200 m are difficult to handle numerically (Hestholm and Ruud, 1993).

The next steps in our analysis were to introduce velocity perturbations in either the mantle lithosphere or in the crust. The corresponding synthetic seismograms are presented in Figs. 2.3.5 and 2.3.6, respectively. A remarkable feature in Fig. 2.3.6 is the relatively strong Pn- and Sn-phases. The velocity perturbations of the medium (a_x = 10 km; a_z= 2.5 km) are seemingly very efficient in scattering energy from the sub-Moho Pn wave up into the crust. Moreover, P-coda comprises mainly P-to-P scattered wavelets from the mantle lithosphere. For the inhomogeneous crust synthetics (Fig. 2.3.7) a rather dramatic effect is the strong smearing of the major phases having their propagation paths within the crust. The extent of waveform deformation is obviously proportional to the path length. As usual, the P coda consists mainly of P-to-P scattered wavelets. P-to-Rg scattering is not very efficient since the free surface is flat, although our models have a low-velocity layer in the top crust as indicated in Fig. 2.3.1. From semblance analysis (these results are not shown), we have that the S-coda is dominated by S-wavelets with average, apparent velocities in the range 4.0-4.5 km s^{-1}. S-waves efficiently convert to P-phases by reflection at the free surface, but regarding scattering from velocity perturbations P-to-S conversions appear more efficient than S-to-P, in agreement with theory (Aki, 1992). However, since P-to-S scattering is most efficient for scattering angles around 90 deg, the P-coda is almost devoid of S-wavelets.

Snapshots for a model where the entire lithosphere has randomized velocity perturbations are shown in Fig. 2.3.8. The lapse times are 20 sec, while the S-source depths are at 2 and 20 km, respectively. A comparison with Fig. 2.3.5 (bottom) convincingly demonstrates the profound smearing effect small-scale structural heterogeneities have on the seismogram even for short propagation distances of around 100 km. Also striking is the effect of focal depth at least for models with a positive velocity gradient in the crust. In other words, for a shallow source, a considerable amount of the signal energy becomes trapped in the uppermost crust. From semblance analysis of the synthetics (results not shown), we have that the S-coda consists mainly of P-to-S and S-to-S scattering wavelets. Some Rg-wavelets were also found in the S-coda, presumably reflecting S-to-Rg scattering from the topographic hills in the model used. This in turn confirms the observational results of

Gupta et al (1993) stemming from f-k analysis of local event recordings at NORSAR. The same smearing effect as seen for S-waves (Fig. 2.3.8) was found for P-waves (not shown).

Discussion

Our basic lithosphere model in Fig. 2.3.3 is simple, essentially a single layer over a halfspace. A drawback in our analysis is that finite-difference synthetics are computationally demanding, thus limiting us to 2D models. A practical consequence of this is that 2D models may give a somewhat simplified picture of the wavefield compared to seismic waves in the real earth, which is 3D. Anyway, perhaps most important is that our synthetics share dominant wavefield characteristics with seismograms stemming from real recordings of local events. For example, for inhomogeneous models (e.g., see Figs. 2.3.7 and 2.3.8), the coda excitation relative to the amplitudes of major P- and S-phases is roughly similar to that in real recordings. Likewise, the P-coda consists mainly of P-wavelets, and the S-coda dominantly of S-wavelets. Some P-to-Rg and S-to-Rg scattering can be found in the P- and S-coda, respectively, in case of rough surface topography. The mentioned smearing of the major P- and S-phases is also seen in real records. A practical consequence is that caution should be exercised in reporting weak secondary phases. Also, the multilayered laterally homogeneous crustal models commonly derived from refraction profiling experiments could probably often be substituted by a simple crustal model with small-scale random velocity perturbations.

In the synthetic seismogram exercises described here, we also included an analysis of the teleseismic coda excitation. This was achieved by placing sensors at a depth of 100 km (details in Fig. 2.3.1). The outcome here was that coda could not be generated in the source area to the extent seen in the teleseismic coda records (Bannister et al, 1990). Further support of this conclusion comes from the fact that S-to-P scattering appears to be weak as demonstrated in the previous section.

Finally, a more comprehensive presentation of the work reported here will appear in a forthcoming paper by Hestholm et al (1993).

E.S. Husebye
B.O. Ruud, Dept. of Geology, Oslo University
S.O. Hestholm, IBM Bergen Environmental Sciences and Solutions Centre

References

Aki, K., (1992): Scattering conversions P to S versus S to P, *Bull. Seism. Soc. Am.*, 82, 1969-1972.

Bannister, S.C., E.S. Husebye and B.O. Ruud (1990): Teleseismic P-coda analyzed by three-component and array techniques: deterministic location of topographic P-to-Rg scattering near the NORESS array, *Bull. Seism. Soc. Am.*, 80, 1969-1986.

Birch, F. (1961): The velocity of compressional waves in rocks to 10 kilobars, Part 2. *J. Geophys. Res.*, 66, 2199-2224.

Charette, E.E. (1991): *Elastic wave scattering in laterally inhomogeneous media*, Ph.D. thesis, MIT, Cambridge, MA, USA, 222 pp.

Frankel, A. and R.W. Clayton (1986): Finite difference simulations of seismic scattering: Implications for the propagation of short-period seismic waves in the crust and models of crustal heterogeneity. *J. Geophys. Res.*, 91, 6465-6489.

Gupta, I.N., C.S. Lynnes and R.A. Wagner (1993): An array study of the effects of a known local scatterer on regional phases, *Bull. Seism. Soc. Am.*, 83, Feb 93.

Hestholm, S.O., B.O. Ruud, E.S. Husebye and B.O. Rosland (1992): Synthesizing 2D wave propagation in a heterogeneous lithosphere using finite difference techniques. In: E.S. Husebye and B.O. Ruud, Seismic Surveillance -- Nuclear test ban verification, Report PL-TR-92-2095, Phillips Laboratory, Hanscom AFB, Massachusetts, USA. **ADA253689**

Hestholm, S.O. and B.O. Ruud (1993): 2D finite difference elastic wave modelling including surface topography, manuscript submitted for publication.

Hestholm, S.O., E.S. Husebye, B.O. Ruud and B.O. Rosland (1993): Visualizing seismic wave propagation in complex crust-upper mantle media using 2D finite difference synthetics, manusript in preparation.

Toksöz, M.N., A.M. Dainty, E. Reiter and R.S. Wu (1988): A model for attenuation and scattering in the earth's crust, *Pure and Appl. Geophys.*, 128, 81-100.

Model	Source		Free Surface			Moho			Crust/Upper Mantle				Remarks
	(P/S)	Depth	v	a	rms	v	a	rms	v	a_x	a_z	rms	
	--	(km)	--	(km)	(km)	--	(km)	(km)	--	(km)	(km)	(%)	
Mod 1	--	--	--	--	--	0.5	10.0	1.0	0.3	10.0	2.5	3.0	Fig 2.3.2
Mod 2	P/S	20	..	--	--	--	--	--					Fig 2.3.3
Mod 3	P/S	20	--	--	--	0.5	10.0	10	--	--	--	--	Fig 2.3.4
Mod 4	P/S	20	1.0	10.0	0.2	0.5	10.0	1.0	--	--	--	--	Fig 2.3.5
Mod 5	P/S	20	--	--	--	--	--	--	0.3	10.0	2.5	3.0	Fig 2.3.6 (mantle)
Mod 6	P/S	20	--	--	--	--	--	--	0.3	10.0	2.5	3.0	Fig 2.3.7 (crust)
Mod 7	S	2/20	1.0	10.0	0.2	--	--	--	0.3	10.0	2.5	3.0	Fig 2.3.8

Table 2.3.1. Listing of crust and mantle lithosphere parameters, supplementary to those in Fig. 2.3.1, for various models used in analysis. The Free Surface, Moho and Crust/ Upper Mantle columns give 1D and 2D von Kármán medium parameters, namely the order u, the correlation distance a (2D: ax and az), and the RMS level (km) and velocity (per cent) perturbations. The rightmost column gives the figure numbers where the corresponding synthetics or snapshots are displayed.
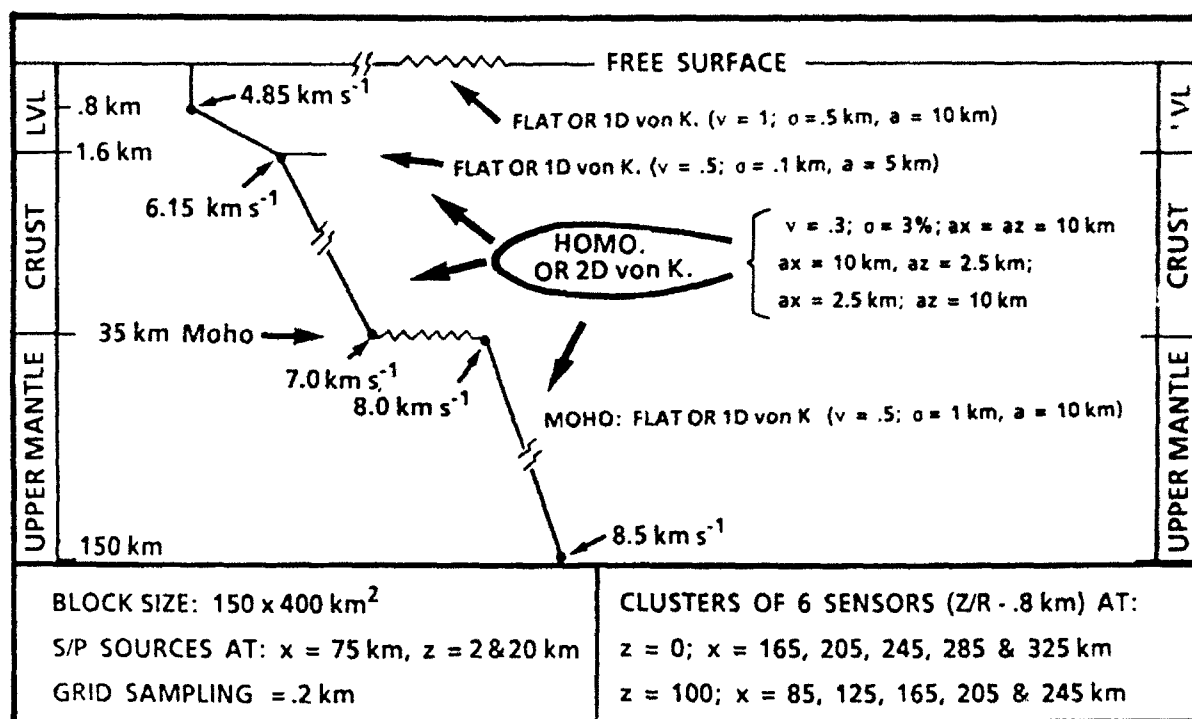
Fig. 2.3.1. The class of crust and upper mantle models used in our generation of 2D finite difference (FD) synthetic seismic records. Specific model choices exclusive layer thicknesses and crust and upper mantle velocity gradients are detailed in Table 2.3.1. Both vertical (Z) and horizontal (R) component seismograms are extracted at 5 groups of 6 sensors each at the free surface and at a depth of 100 km. The grop sensor spacing is 0.8 km and further configuration details in the lower right box. Block size and source positions are detailed in the lower left box. Note that the minimum horizontal distances between the source and the closest sensor grouping (A0) are 90 km (surface) and 10 km (100 km depth).
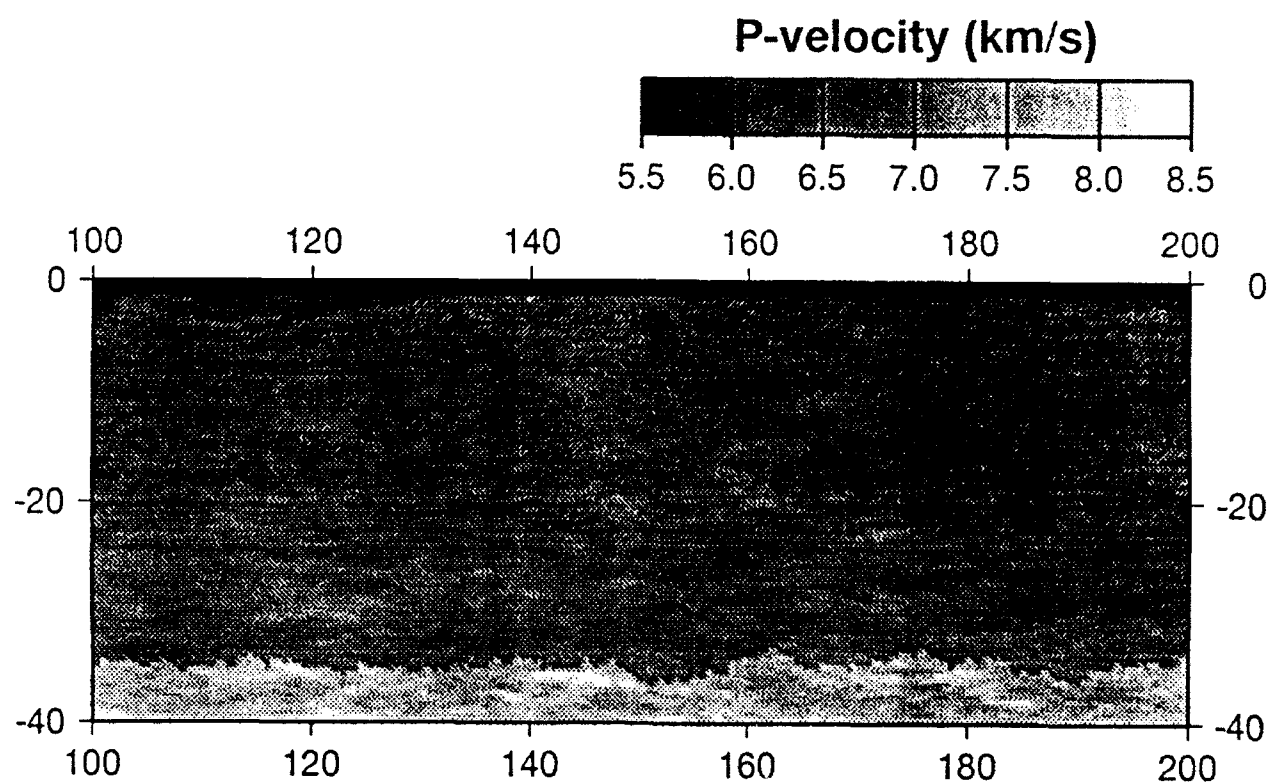
Fig. 2.3.2. P-velocity fluctuations in the crust and upper mantle for a 40 x 100 km^2 subset of the basic model shown in Fig. 2.3.1. These are realizations of an inhomogeneous medium without ($a_x = a_z = 10$ km) and with so-called spatial anisotropy with $a_x = 10$ km and $a_z = 2.5$ km. Further details are given in Table 2.3.1 (Mod 1). Typcial model features are a top crust low velocity layer, the black rim in the figures, and a corrugated Moho of enhanced visibility due to the velocity jump across the interface.
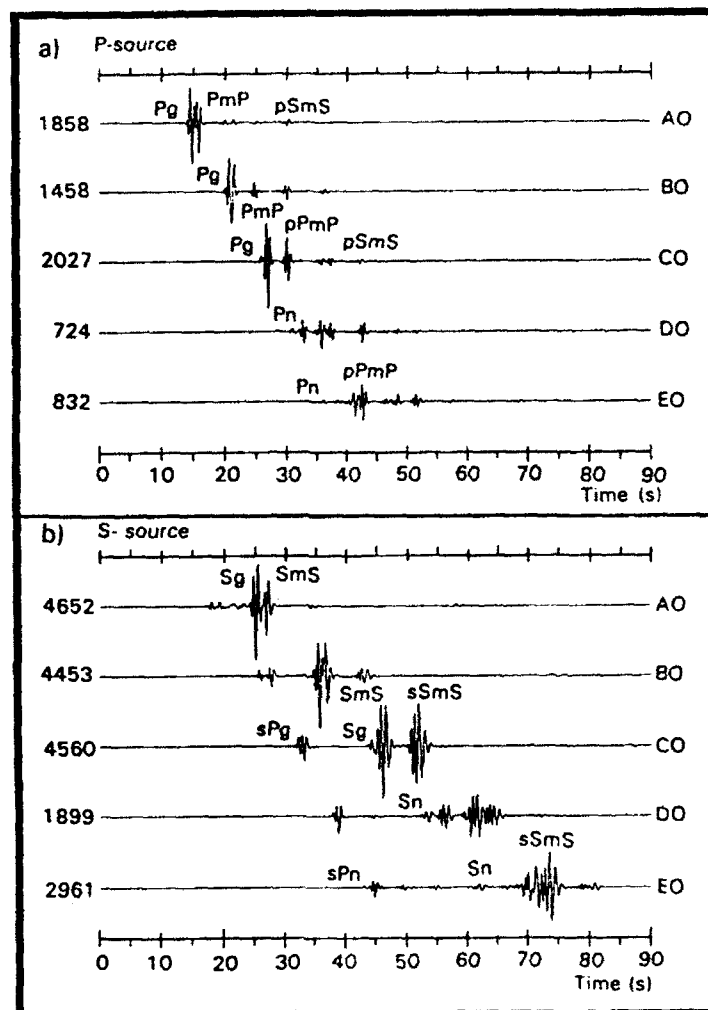
Fig. 2.3.3. The P- and S-source synthetic seismograms (Z-components) shown in a) and
b), respectively, are for a homogeneous medium, that is, Model 2 in Table 2.3.1.
Common features are a source depth of 20 km and that only the first sensor trace
from each of the 5 clusters at the surface are shown (details in the lower right box in
Fig. 2.3.1). These synthetics, including phase designations, are similar to those gen-
erated by ray tracing techniques -- sharp and clear without coda wavelets. Adding
figures a) and b) would give synthetics similar to those stemming from an earth-
quake source (except for radiation pattern).
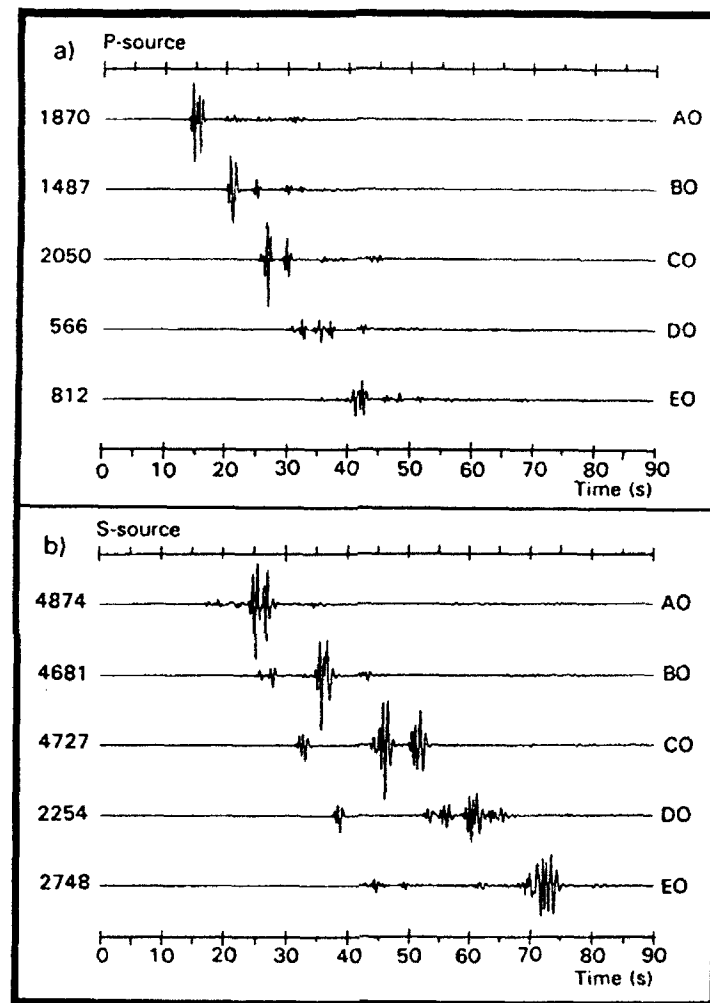
Fig. 2.3.4. P- and S-source synthetics in a) and b), respectively, for a laterally homogeneous model but with a corrugated Moho (Model 3 in Table 2.3.1). A comparison with Fig. 2.3.3 gives that Moho undulations contribute little to the free surface coda (Z-component). This also applies to the S-waves which dominate wavelengths close to those of the Moho undulations. As before, A0, ..., E0 are first sensors in each cluster at the free surface; horizontal spacing in the lower right box in Fig. 2.3.1.

Vertical particle velocity
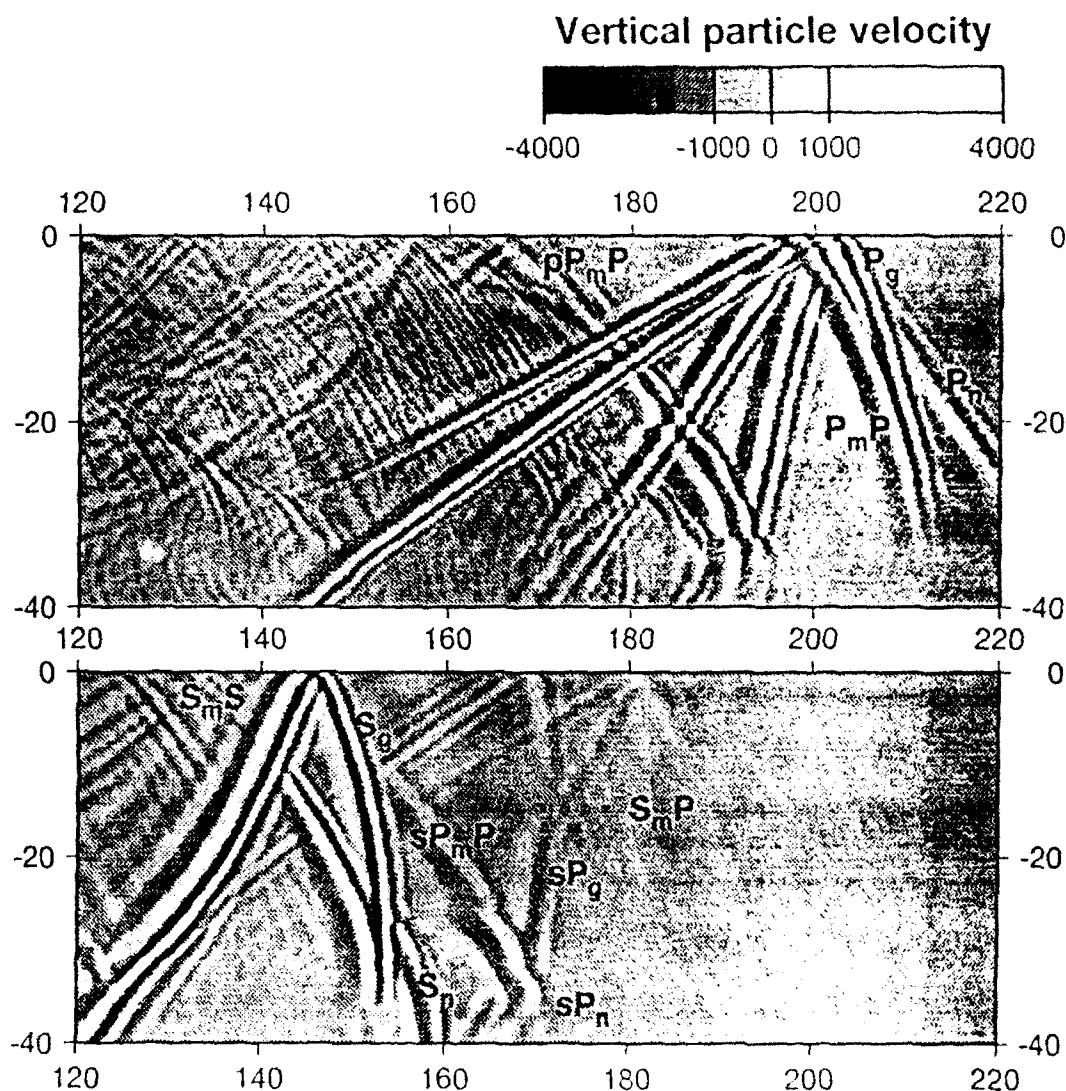
Fig. 2.3.5. Snapshot displays at a lapse time of 20 sec for P- and S-sources at 20 km depth and embedded in a unperturbed medium with a corrugated Moho and free surface topography (Model 4 in Table 2.3.1). Even for such a simple source and medium, the corresponding wavefields are quite complex; in order to facilitate their interpretations, major up-going phases are labelled. Down-going reflections from the free surface are not marked due to a lack of a specific nomenclature here for local distances. The efficiency of P-to-Rg conversions at the surface is obvious and appears as a grey/white banding in the top crust.
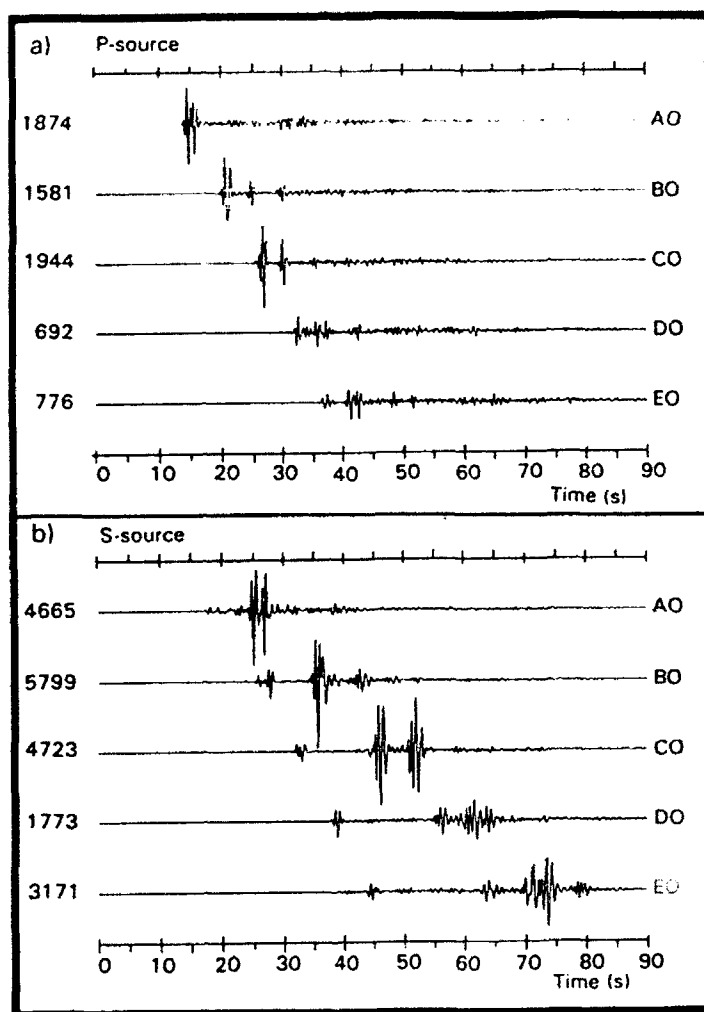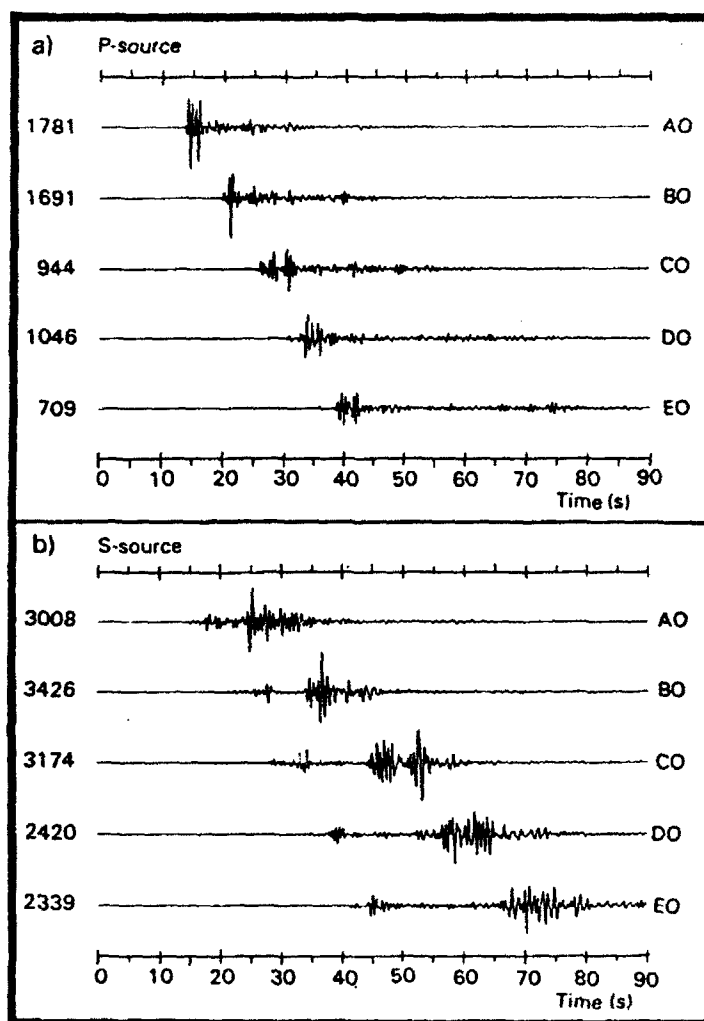
Fig. 2.3.6. P- and S-source synthetics in a) and b), respectively, for a laterally homogeneous model except that the upper mantle velocities are perturbed (Model 5 in Table 2.3.1). In comparison to Fig. 2.3.3 the crustal phases are little deformed, while the Pn and Sn phases on trace EO are strong and appear to be "shifted" approx. 1 sec in time. The most striking feature is the relatively strong coda reflecting first order back-scattering contributions from sub-Moho inhomogeneities. The P-coda (until the first S-arrival) consists mainly of P-wavelets and then S-wavelets dominate.

Fig. 2.3.7. P- and S-source synthetics in a) and b), respectively for a laterally homogeneous model except that the velocities in the crustal part are perturbed (Model 6 in Table 2.3.1). In comparison to Figs. 2.3.3 and 2.3.6, the crustal phases like Pg and Sg (Lg) are strongly deformed. Also, b) demonstrates why Sn-phases relatively seldom are reported: they are simply lost in the P-coda.
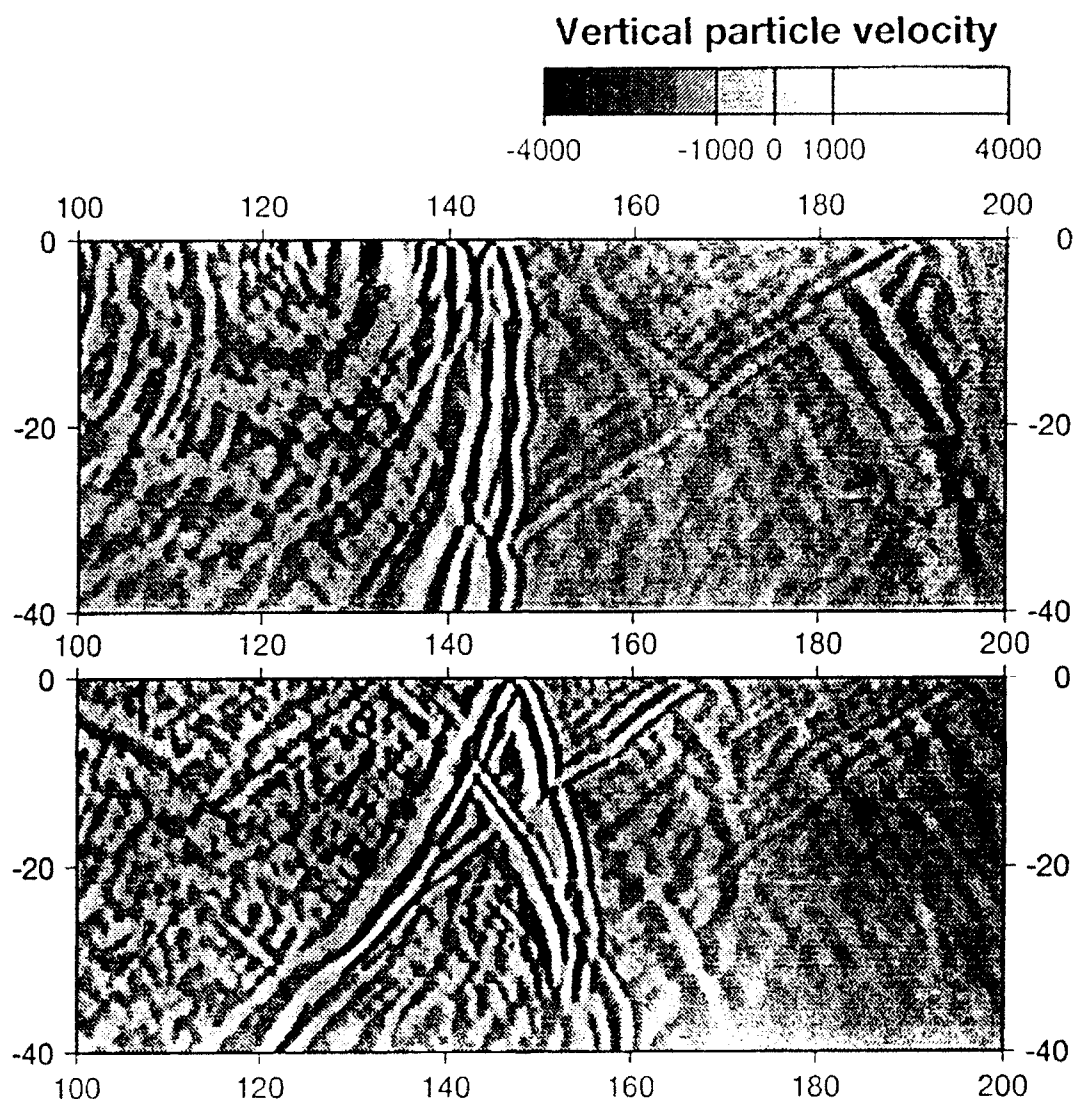
Vertical particle velocity

Fig. 2.3.8. Snapshot displays at a lapse time of 20 sec (Model 7 in Table 2.3.1) for S-sources at depths of 2 (top) and 20 km (bottom). In comparison to Fig. 2.3.5 (bottom part, same configuration), we see that only the strongest S-phases are retained intact. The SmS-phase is well preserved in the middle crust, but strongly weakened at the surface -- where the seismometers are located. For the shallow source (top) relatively much wave energy is confined to the top crust.

2.4   Status of development of the Northern Europe Regional Array Network

Data from the Northern Europe Regional Array Network have formed the basis for much of the research reported on in this contract, and it should be of interest to summarize the current status of development of this network.

As of November 1992, the configuration of the network is as shown in Fig. 2.4.1. The six small-aperture arrays contributing data to the NORSAR Data Processing Center at Kjeller are the NORESS and ARCESS arrays in Norway, FINESA in Finland, GERESS in Germany, as well as the newly installed arrays at Apatity on the Kola Peninsula of Russia, and near Longyearbyen on the Arctic island of Spitsbergen. Details on the latter two arrays are given in the following.

A new small-aperture array near Apatity, Russia

The scientific cooperation between NORSAR and the Kola Science Centre of the Russian Academy of Sciences started in June 1991 with the installation of a digital, high-quality three-component seismic station in Apatity on the Kola Peninsula of Russia. This cooperation was considerably expanded through the installation during the summer and fall of 1992 of a dedicated full duplex 64 kbps satellite link between the Kola Regional Seismological Centre (KRSC) in Apatity and NORSAR at Kjeller, several Sun workstations for data acquisition and analysis as well as a three-component broad band station at KRSC, and a small-aperture array outside Apatity.

The Apatity station was installed in September approximately 17 km to the west of KRSC in Apatity, at the location indicated in Fig. 2.4.2. The geometry of the array is shown in Fig. 2.4.3. The instruments are placed on two concentric rings plus one in the center, and the aperture is approximately 1 km. All sites are equipped by a short period vertical seismometer of type Geotech S-500, and the site at the center of the array has in addition two horizontal seismometers of the same type.

The data from the new array are digitized at the central array site and then transmitted via three radio channels to Apatity where a NORAC array controller (Paulsen, 1992) collects and timetags the data. The digitizers used are of types Nanometrics three-channel RD-3 and six-channel RD-6, which are both 16-bit converters with gain ranging. Short-period data from the nine vertical sensors of the array are sampled at 40 Hz. Data from the three seismometers at site A0 are sampled at 80 Hz, thus providing a high-frequency three-component station integrated with the array. The seismic data from the vertical sensor at site A0 are thus sampled both at 40 Hz (and used in the processing together with the vertical sensors of the A- and B-rings) and at 80 Hz (and used as part of the high-frequency thee-component station). The three-component broad band seismometer installed on the pier of the basement of the building of the KRSC in Apatity is of type Guralp CMG-3T, and the data are digitized using a Nanometrics RD-3 digitizer. Timing is provided throughout the system on the basis of reception of GPS signals.

Fig. 2.4.4 shows the current configuration of the data acquisition and analysis system at the KRSC. The figure shows the local Ethernet established, the NORAC array controller that receives data from the four digitizers, three Sun Sparcstations (kan, imandra and umb) and a Sun X-terminal, and the Cisco router that provides the gateway connection to NOR-SAR via the dedicated satellite link. IDU is the satellite indoor unit containing the modem and other communications equipment. The system described in Fig. 2.4.4 allows the staff at the KRSC to perform on-line processing as well as interactive analysis of the data recorded at Apatity. Using the satellite link, all data recorded at NORSAR from the other arrays of the network can also be retrieved by the KRSC personnel.

The overall picture related to the Apatity developments is given in Fig. 2.4.5. It shows that the data acquired in Apatity and retrieved via the NORSAT B satellite link are made available to the Intelligent Monitoring System (IMS) at NORSAR. Additional details on the Apatity developments can be found in Mykkeltveit et al (1992).

Preliminary analysis of data from the new Apatity array has been conducted by Ringdal and Fyen (1992). They conclude that the Apatity array is at least as efficient in suppressing noise between 1 and 5 Hz as the corresponding NORESS subgeometry. It thus appears that the spatial noise characteristics at Apatity are similar to those found in other areas of Fennoscandia and the Baltic Shield. They also conclude that the Apatity array has a higher noise level than ARCESS at frequencies above 2 Hz, whereas the noise levels are similar at lower frequencies. On the other hand, they find that the noise level is considerably lower than that of the station located at the KRSC in the town of Apatity.

A new small-aperture array on the Arctic island of Spitsbergen

A small-aperture array very similar to the Apatity array described above was installed on the island of Spitsbergen (Fig. 2.4.1) during late October/early November 1992. The implementation of this array was supported financially by Oljeindustriens Landsforening (OLF), which is an association of oil companies taking part in oil exploration and production on the Norwegian Continental Shelf. The establishment and operation of the communications channels needed in order to integrate the Spitsbergen array data into IMS is supported by DARPA.

A suitable location for the Spitsbergen array was found during a site-selection survey in August 1991. The site is located on Janssonhaugen in Adventdalen approximately 15 km east-southeast of Longyearbyen (see Fig. 2.4.6), which is the largest Norwegian settlement and also administrative center on the island. Janssonhaugen is a hill in the middle of a valley (Adventdalen), and the array is deployed on the plateau of this hill. The rocks at the site are of Cretaceous aag, covered by thin moraine of variable depth. The sensors are placed at the bottom of 6 m deep cased boreholes. The bottom of the boreholes are either in Cretaceous rock or in moraine material in stable permafrost conditions (temperature approximately -5^{0}C all year round at a depth of 6 m), such that there is no melting/freezing taking place at this depth.

The geometry of the Spitsbergen array is very similar to that of the Apatity array. Nine sensor sites distributed over an array aperture of approximately 1 km are equipped with

short-period vertical seismometers of type Geotech S-500. A broad band three-component seismometer of type Guralp CMG-3T is planned for installation in 1993. Power at the Spitsbergen array is provided through the use of two windmills which deliver 12 V DC through a battery bank. Data from two Nanometrics RD-6 digitizers located at the array site are transmitted over two radio links to Longyearbyen, where the data are entered into a NORAC array controller. From Longyearbyen, the Spitsbergen array data are transmitted via a terrestrial link to Norwegian Telecom's satellite hub station at Isfjord Radio, from where a simplex 64 Kbits/s satellite link is used for transmission of continuous data to Norway.

Data processing using the IMS

IMS (Bache et al, 1990) was installed at NORSAR in December 1989 and was operated at NORSAR from 1 January 1990 for automatic processing of data from ARCESS and NORESS. A second version of IMS that accepts data from an arbitrary number of arrays and single 3-component stations was installed at NORSAR in October 1991, and regular operation of the system comprising analysis of data from the 4 arrays ARCESS, NORESS, FINESA and GERESS started on 15 October 1991. As opposed to the first version of IMS, the one in current operation also locates events at teleseismic distance.

The overall performance of IMS is very satisfactory. In order, however, to achieve further improvements to the IMS, NORSAR analyst and seismologist staffs are involved in evaluating the performance of IMS when new versions of IMS are released by SAIC, the systems developer. Such evaluations focus on the performance of the automatic phase association and event location algorithms used and make use of several independent bulletins.

The integration of data from the Apatity array in IMS has been rather straightforward. The seismic wave propagation characteristics in the areas around this array are similar to those found in other parts of Fennoscandia, and it has not been necessary to implement specific "rules" for this array in order to achieve reasonable performance . On the other hand, the integration of data from the Spitsbergen array is expected to presented interesting seismological challenges, as this array is located in an area of much younger geology than the other five arrays.

S. Mykkeltveit

References

Bache, T.C., S.R. Bratt, J. Wang, R.M. Fung, C. Kobryn and J.W. Given (1991): The intelligent monitoring system, *Bull. Seism. Soc. Am.,* 80, Part B, 1852-1873.

Krementskaya, E.O. (1991): Contemporary seismicity of the NW part of the USSR, *Semi-ann. Tech. Summ. 1 April - 30 September 1991*, NORSAR Sci. Rep. No. 1-91/92.

Mykkeltveit, S., A. Dahle, J. Fyen, T. Kværna, P.W. Larsen, R. Paulsen, F. Ringdal and I. Kuzmin (1992): Extensions of the Northern Europe Regional Array Network -- New small-aperture arrays at Apatity, Russia, and on the Arctic island of Spitsbergen, *Semiann. Tech. Summ. 1 April - 30 September 1992*, NORSAR Sci. Rep. No. 1-92/93, Kjeller, Norway.

Paulsen, R. (1992): NORAC: A new array controller, *Semiann. Tech. Summ. 1 October 1991 - 31 March 1992*, NORSAR Sci. Rep. No. 2-91/92, Kjeller, Norway.

Ringdal, F. and J. Fyen (1992): Initial processing results from the Apatity small-aperture array, *Semiann. Tech. Summ. 1 April - 30 September 1992*, NORSAR Sci. Rep. No. 1-92/93, Kjeller, Norway.
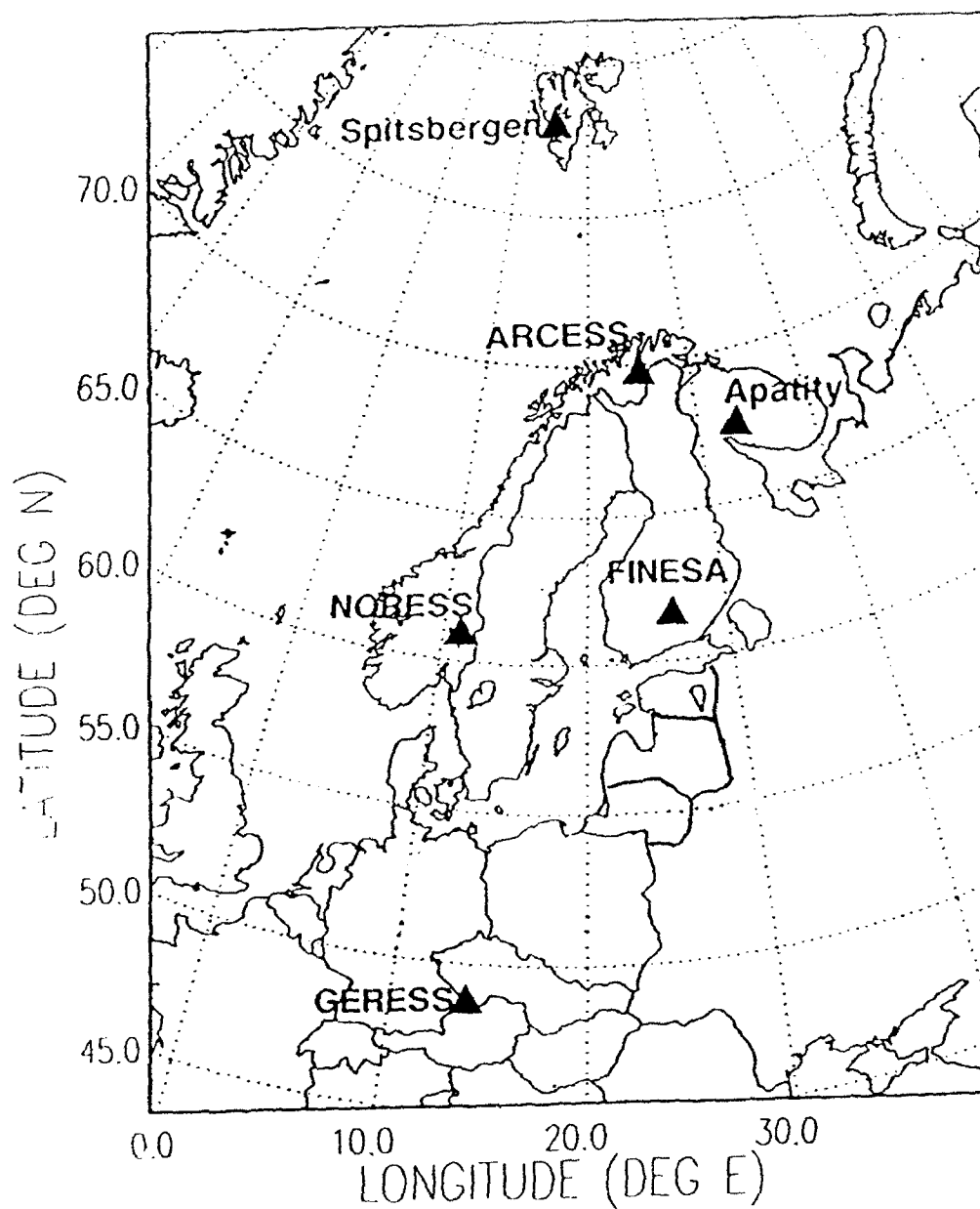
Fig. 2.4.1. The figure shows the stations of the Northern Europe Regional Array Network as of November 1992. All stations of the network are small-aperture arrays.
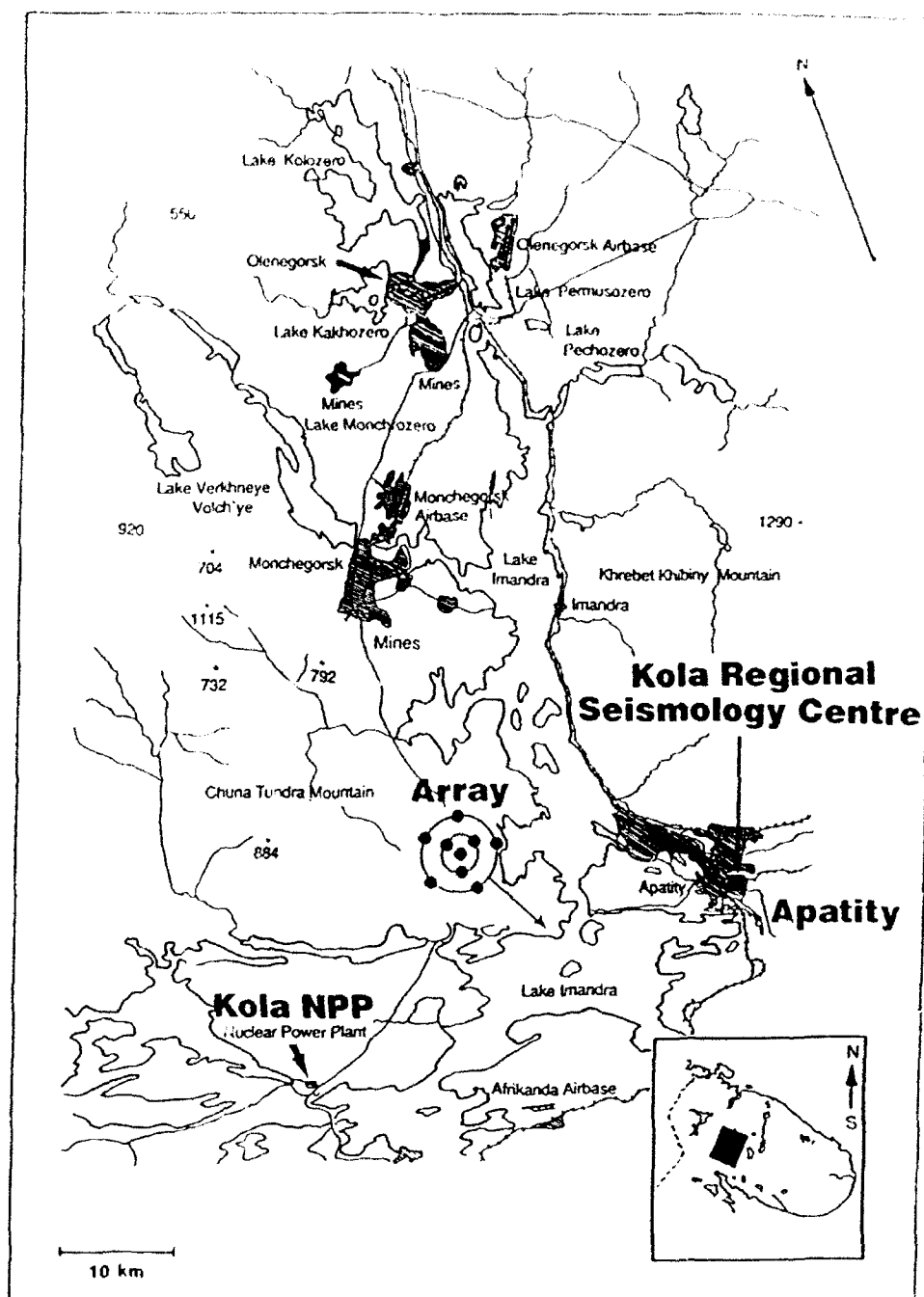
Fig. 2.4.2. Map of the Apatity region on the Kola Peninsula of Russia, showing the location of the Kola Regional Seismology Centre and the location of the new small-aperture array (not drawn to scale; the array aperture is 1 km). Also shown are the mining areas in Monchegorsk and Olenegorsk to the north of the array. The seismicity in the area, and in particular the seismicity associated with the mining activity in the Khibiny Mountain area to the north of Apatity, is described in Kremenetskaya (1991).
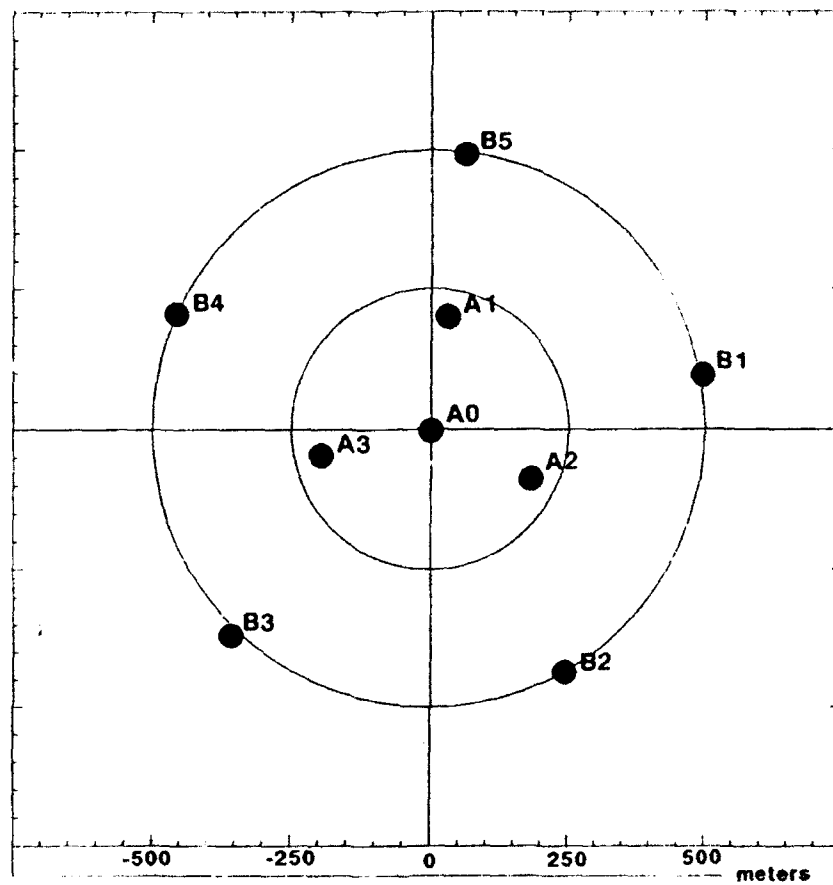
Fig. 2.4.3. Configuration of the new Apatity small-aperture array.
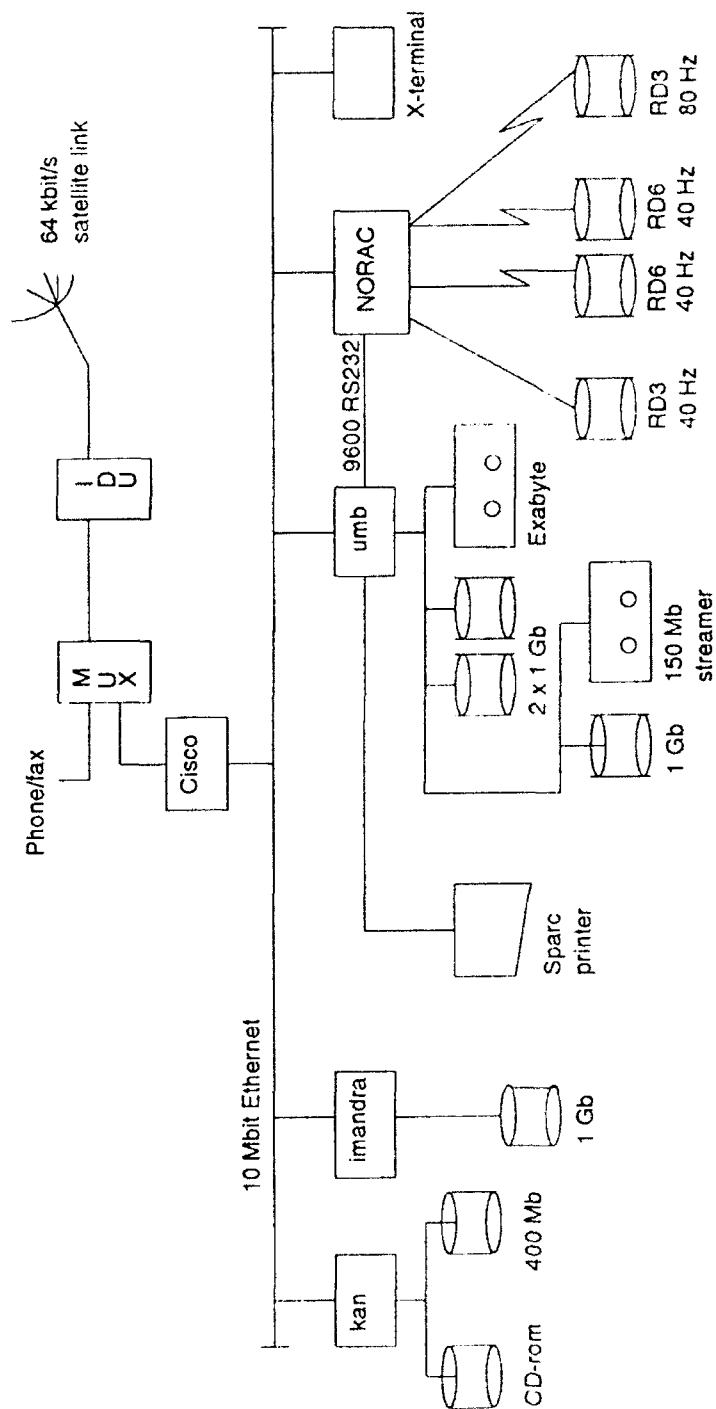
Fig. 2.4.4.. The figure shows the configuration of the computer system installed at the Kola Regional Seismology Centre in Apatity. Also shown is the network connection to NORSAR via the dedicated 64 kbits s satellite link.
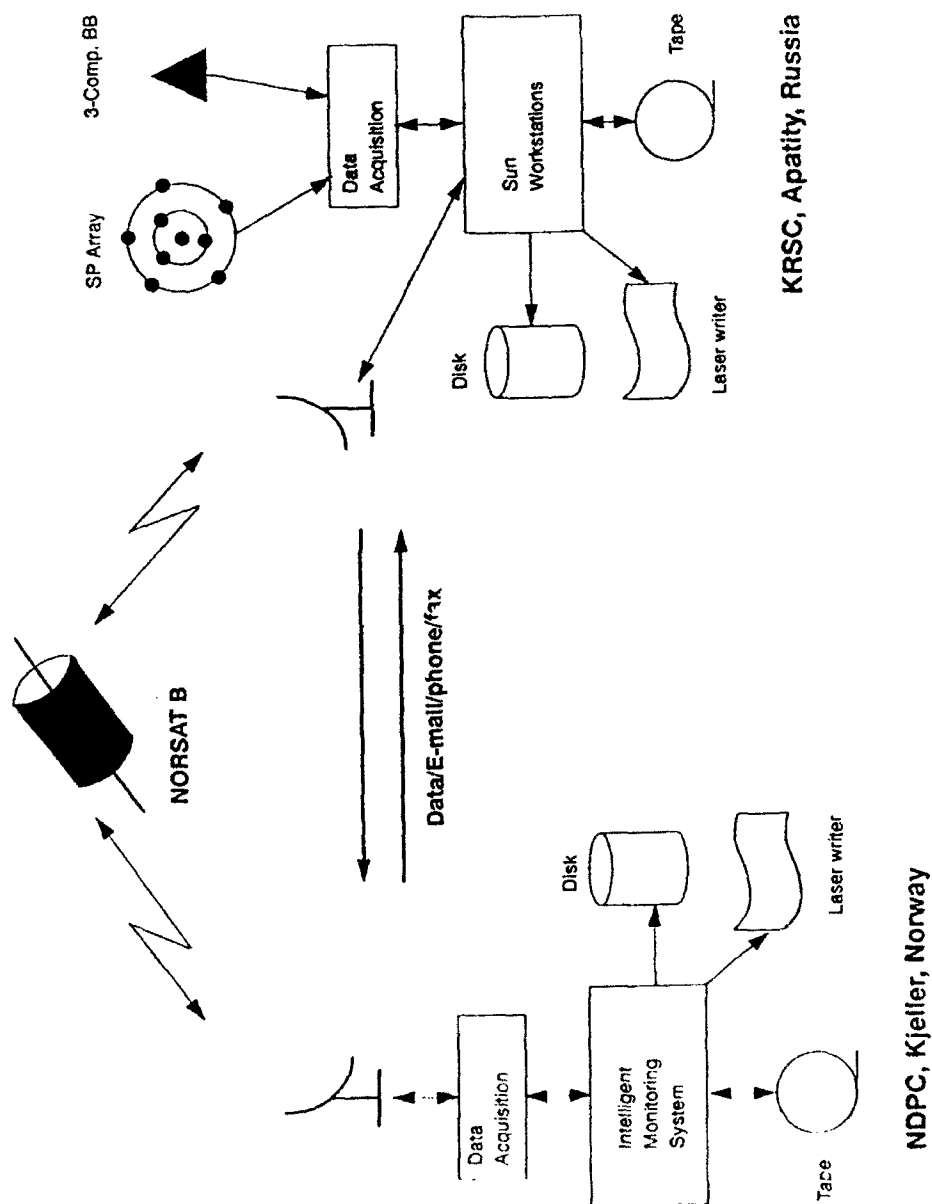
Fig. 2.4.5. Schematic overview of the field installations and computer system in Apatity and the interfacing with the NORSAR Data Processing Center (NDPC) in Norway via the NORSAT B satellite link.
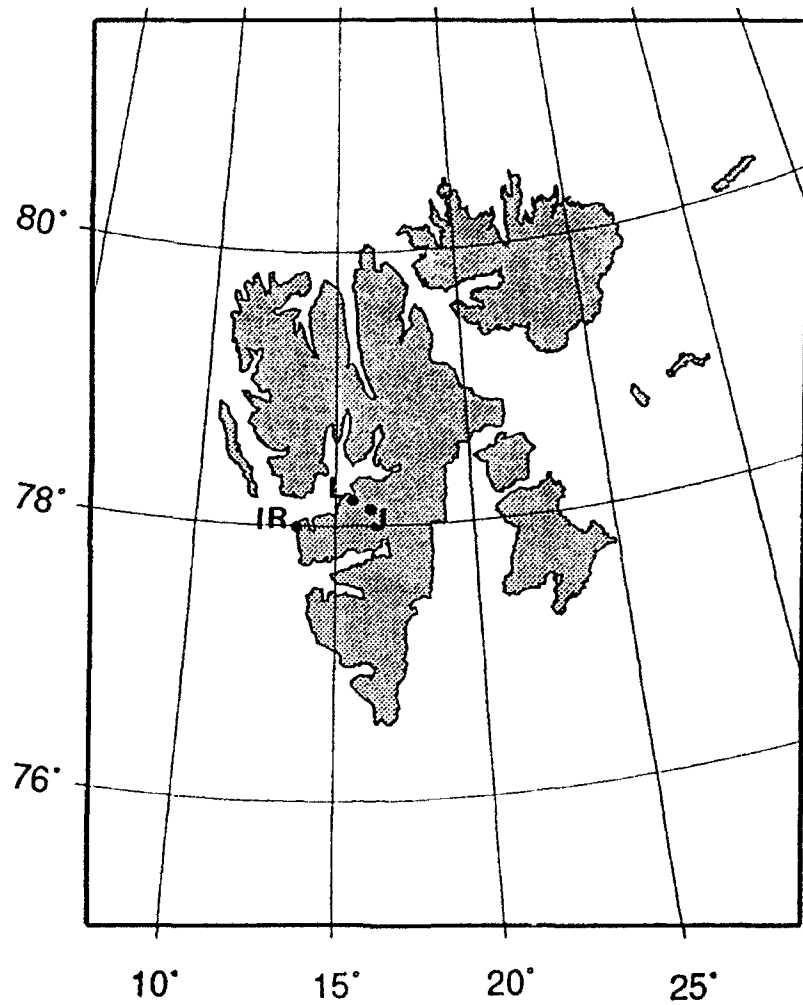
Fig. 2.4.6. This map of the Svalbard archipelago with its main island Spitsbergen shows
the location of the array site at Janssonhaugen (J), the location of the array controller
at Norwegian Telecom's facility at Longyearbyen (L), and the location of the NOR-
SAT B earth station at Isfjord Radio (IR).

2.5   Summaries of Quarterly Technical Reports submitted

During FY92, three quarterly technical reports have been submitted on this contract. The abstracts of these papers are given in the following.

2.5.1   Continuous seismic threshold monitoring of the northern Novaya Zemlya test site; long-term operational characteristics -- T. Kværna

In this work we demonstrate the practical capability of the Continuous Seismic Threshold Monitoring method to monitor the northern Novaya Zemlya test site at a very low threshold over an extended time period, using data from the Fennoscandian array network (NORESS, ARCESS and FINESA). We show that during February 1992 the network based magnitude threshold, at the 90% confidence level, stays below $m_b = 2.50$, 99.72% of the time. We further "explain" all peaks in the network magnitude thresholds exceeding $m_b = 2.6$ as resulting from interfering signals from an identified seismic event (teleseismic or regional), or a short outage of the most important array (ARCESS). We also argue that this implies that at the given confidence level, there has been no seismic event of $m_b \geq 2.6$ at the northern Novaya Zemlya test site during February 1992.

During normal conditions, i.e., when the network threshold is low, ARCESS is clearly the most important array, followed by NORESS and FINESA. But during time periods when the ARCESS noise level is high, or when there are interfering events, the relative contribution of NORESS and FINESA increases significantly. The redundancy resulting from the use of several arrays is also essential during outages of one or more of the arrays.

The threshold magnitudes for each array during background noise conditions are close to normally distributed, at least within shorter time intervals. Small deviations from the normal distribution occur because of long-term fluctuations in the background noise level. The average magnitude thresholds at FINESA exhibit strong weekly and diurnal variations. The latter are particularly significant on workdays. The average NORESS thresholds show rather small variations, whereas at ARCESS, large variations of more than $0.5 \ m_b$ units are observed. The causes of the peak periods at ARCESS are most likely severe wind and weather conditions.

2.5.2   Continuous Seismic Threshold Monitoring -- F. Ringdal and T. Kværna

Continuous threshold monitoring is a technique for using a seismic network to monitor a geographical area continuously in time. The method provides, at a given confidence level, a continuous assessment of the upper magnitude limit of possible seismic events that might have occurred in the target area. Two approaches are presented in this paper.

Site-specific threshold monitoring: By "focusing" a seismic network on a specific target site, continuous threshold monitoring of that site is achieved. We optimize the monitoring capability by tuning the frequency filters and array beams to known characteristics from previously recorded events at the site. We define the *threshold trace* for the network as the continuous time trace of computed upper magnitude limits of seismic events in the target area, at a 90% confidence level. As an example, we have conducted a one-week monitor-

ing experiment of the northern Novaya Zemlya nuclear test site, using the Fennoscandian regional array network (NORESS, ARCESS, FINESA). We find that the threshold trace is below $m_b = 2.5$ more than 99% of the time. Thirty-four peaks exceed $m_b = 2.5$. All of these peaks correspond to seismic events that have been independently located by a teleseismic or regional network. During the entire one-week time period, the threshold trace exceeded $m_b = 2.5$ only for 43 minutes.

Regional threshold monitoring: This involves conducting site-specific monitoring of a dense grid of geographical aiming points and requires the development of generic phase attenuation relationships for covering an extended geographical region. Using again the Fennoscandian regional array network, we illustrate the regional threshold monitoring approach by maps with color contour displays. We demonstrate that the network thresholds in Fennoscandia and adjacent regions show strong regional dependence. The thresholds are below $m_b = 0.5$ close to each array (< 300 km distance) and range from $m_b = 2.0$ to 2.5 in parts of the Norwegian Sea and Barents Sea. The thresholds also vary significantly under different background noise conditions, and an increase of about 1.0 m_b units is observed during a large teleseismic earthquake. These regional threshold maps have advantages over standard network capability maps in being more accurate during time intervals when interfering seismic events occur. They can also more easily reflect special conditions such as particularly favorable source-station propagation paths, and have the advantage of not being tied to specific event detection criteria.

The paper concludes that continuous threshold monitoring offers a valuable supplement to traditional seismic techniques used in nuclear test ban monitoring. The method may also be useful for monitoring earthquake activity at low magnitudes for sites of special interest, as well as for monitoring earthquake aftershock sequences.

2.5.3 Mining explosions in the Khibiny Massif (Kola Peninsula of Russia) recorded at the Apatity three-component station -- S. Mykkeltveit

This report offers a description of the three-component seismic station that was installed in Apatity on the Kola Peninsula of Russia in June of 1991. Data from this station are useful for studying mining explosions in the nearby Khibiny Massif. Colleagues at the Kola Regional Seismological Centre in Apatity have provided us with detailed information on 200 mining explosions undertaken during June 1991 - September 1992, and we have compiled a data base comprising data from 61 of these explosions. The data are used to estimate the noise level at the Apatity station, and also for estimation of P-wave arrival azimuths, using a broad band slowness analysis technique. Values for the true azimuths are available from information presented in this report, and the azimuth residuals are found to have a median value of -7.06 degrees. A small-aperture array was installed close to Apatity in the fall of 1992, and some perspectives for the future use of data from Apatity are discussed.

1.

Marvin Denny
U.S. Department of Energy
Office of Arms Control
Washington, DC 20585

Dr. Cliff Frolich
Institute of Geophysics
8701 North Mopac
Austin, TX 78759

Dr. Zoltan Der
ENSCO, Inc.
5400 Port Royal Road
Springfield, VA 22151-2388

Dr. Holly Given
IGPP, A-025
Scripps Institute of Oceanography
University of California, San Diego
La Jolla, CA 92093

Prof. Adam Dziewonski
Hoffman Laboratory, Harvard University
Dept. of Earth Atmos. & Planetary Sciences
20 Oxford Street
Cambridge, MA 02138

Dr. Jeffrey W. Given
SAIC
10260 Campus Point Drive
San Diego, CA 92121

Prof. John Ebel
Department of Geology & Geophysics
Boston College
Chestnut Hill, MA 02167

Dr. Dale Glover
Defense Intelligence Agency
ATTN: ODT-1B
Washington, DC 20301

Eric Fielding
SNEE Hall
INSTOC
Cornell University
Ithaca, NY 14853

Dr. Indra Gupta
Teledyne Geotech
314 Montgomery Street
Alexanderia, VA 22314

Dr. Mark D. Fisk
Mission Research Corporation
735 State Street
P.O. Drawer 719
Santa Barbara, CA 93102

Dan N. Hagedon
Pacific Northwest Laboratories
Battelle Boulevard
Richland, WA 99352

Prof Stanley Flatte
Applied Sciences Building
University of California, Santa Cruz
Santa Cruz, CA 95064

Dr. James Hannon
Lawrence Livermore National Laboratory
P.O. Box 808
L-205
Livermore, CA 94550

Dr. John Foley
NER-Geo Sciences
1100 Crown Colony Drive
Quincy, MA 02169

Dr. Roger Hansen
HQ AFTAC/TTR
130 South Highway A1A
Patrick AFB, FL 32925-3002

Prof. Donald Forsyth
Department of Geological Sciences
Brown University
Providence, RI 02912

Prof. David G. Harkrider
Seismological Laboratory
Division of Geological & Planetary Sciences
California Institute of Technology
Pasadena, CA 91125

Dr. Art Frankel
U.S. Geological Survey
922 National Center
Reston, VA 22092

Prof. Danny Harvey
CIRES
University of Colorado
Boulder, CO 80309

Prof. Donald V. Helmberger
Seismological Laboratory
Division of Geological & Planetary Sciences
California Institute of Technology
Pasadena, CA 91125

Prof. Eugene Herrin
Institute for the Study of Earth and Man
Geophysical Laboratory
Southern Methodist University
Dallas, TX 75275

Prof. Robert B. Herrmann .
Department of Earth & Atmospheric Sciences
St. Louis University
St. Louis, MO 63156

Prof. Lane R. Johnson
Seismographic Station
University of California
Berkeley, CA 94720

Prof. Thomas H. Jordan
Department of Earth, Atmospheric &
  Planetary Sciences
Massachusetts Institute of Technology
Cambridge, MA 02139

Prof. Alan Kafka
Department of Geology & Geophysics
Boston College
Chestnut Hill, MA 02167

Robert C. Kemerait
ENSCO, Inc.
445 Pineda Court
Melbourne, FL 32940

Dr. Karl Koch
Institute for the Study of Earth and Man
Geophysical Laboratory
Southern Methodist University
Dallas, Tx 75275

Dr. Max Koontz
U.S. Dept. of Energy/DP 5
Forrestal Building
1000 Independence Avenue
Washington, DC 20585

Dr. Richard LaCoss
MIT Lincoln Laboratory, M-200B
P.O. Box 73
Lexington, MA 02173-0073

Dr. Fred K. Lamb
University of Illinois at Urbana-Champaign
Department of Physics
1110 West Green Street
Urbana, IL 61801

Prof. Charles A. Langston
Geosciences Department
403 Deike Building
The Pennsylvania State University
University Park, PA 16802

Jim Lawson, Chief Geophysicist
Oklahoma Geological Survey
Oklahoma Geophysical Observatory
P.O. Box 8
Leonard, OK 74043-0008

Prof. Thorne Lay
Institute of Tectonics
Earth Science Board
University of California, Santa Cruz
Santa Cruz, CA 95064

Dr. William Leith
U.S. Geological Survey
Mail Stop 928
Reston, VA 22092

Mr. James F. Lewkowicz
Phillips Laboratory/GPEH
29 Randolph Road
Hanscom AFB, MA 01731-3010(2 copies)

Mr. Alfred Lieberman
ACDA/VI-OA State Department Building
Room 5726
320-21st Street, NW
Washington, DC 20451

Prof. L. Timothy Long
School of Geophysical Sciences
Georgia Institute of Technology
Atlanta, GA 30332

Dr. Randolph Martin, III
New England Research, Inc.
76 Olcott Drive
White River Junction, VT 05001

Dr. Robert Masse
Denver Federal Building
Box 25046, Mail Stop 967
Denver, CO 80225

3

Dr. Gary McCartor
Department of Physics
Southern Methodist University
Dallas, TX 75275

Dr. Bao Nguyen
HQ AFTAC/TTR
130 South Highway A1A
Patrick AFB, FL 32925-3002

Prof. Thomas V. McEvilly
Seismographic Station
University of California
Berkeley, CA 94720

Prof. John A. Orcutt
IGPP, A-025
Scripps Institute of Oceanography
University of California, San Diego
La Jolla, CA 92093

Dr. Art McGarr
U.S. Geological Survey
Mail Stop 977
U.S. Geological Survey
Menlo Park, CA 94025

Prof. Jeffrey Park
Kline Geology Laboratory
P.O. Box 6666
New Haven, CT 06511-8130

Dr. Keith L. McLaughlin
S-CUBED
A Division of Maxwell Laboratory
P.O. Box 1620
La Jolla, CA 92038-1620

Dr. Howard Patton
Lawrence Livermore National Laboratory
L-025
P.O. Box 808
Livermore, CA 94550

Stephen Miller & Dr. Alexander Florence
SRI International
333 Ravenswood Avenue
Box AF 116
Menlo Park, CA 94025-3493

Dr. Frank Pilotte
HQ AFTAC/TT
130 South Highway A1A
Patrick AFB, FL 32925-3002

Prof. Bernard Minster
IGPP, A-025
Scripps Institute of Oceanography
University of California, San Diego
La Jolla, CA 92093

Dr. Jay J. Pulli
Radix Systems, Inc.
201 Perry Parkway
Gaithersburg, MD 20877

Prof. Brian J. Mitchell
Department of Earth & Atmospheric Sciences
St. Louis University
St. Louis, MO 63156

Dr. Robert Reinke
ATTN: FCTVTD
Field Command
Defense Nuclear Agency
Kirtland AFB, NM 87115

Mr. Jack Murphy
S-CUBED
A Division of Maxwell Laboratory
11800 Sunrise Valley Drive, Suite 1212
Reston, VA 22091 (2 Copies)

Prof. Paul G. Richards
Lamont-Doherty Geological Observatory
 of Columbia University
Palisades, NY 10964

Dr. Keith K. Nakanishi
Lawrence Livermore National Laboratory
L-025
P.O. Box 808
Livermore, CA 94550

Mr. Wilmer Rivers
Teledyne Geotech
314 Montgomery Street
Alexandria, VA 22314

Dr. Carl Newton
Los Alamos National Laboratory
P.O. Box 1663
Mail Stop C335, Group ESS-3
Los Alamos, NM 87545

Dr. George Rothe
HQ AFTAC/TTR
130 South Highway A1A
Patrick AFB, FL 32925-3002

Dr. Alan S. Ryall, Jr.
DARPA/NMRO
3701 North Fairfax Drive
Arlington, VA 22209-1714

Dr. Richard Sailor
TASC, Inc.
55 Walkers Brook Drive
Reading, MA 01867

Prof. Charles G. Sammis .
Center for Earth Sciences
University of Southern California
University Park
Los Angeles, CA 90089-0741

Prof. Christopher H. Scholz
Lamont-Doherty Geological Observatory
 of Columbia University
Palisades, NY 10964

Dr. Susan Schwartz
Institute of Tectonics
1156 High Street
Santa Cruz, CA 95064 ·

Secretary of the Air Force
(SAFRD)
Washington, DC 20330

Office of the Secretary of Defense
DDR&E
Washington, DC 20330

Thomas J. Sereno, Jr.
Science Application Int'l Corp.
10260 Campus Point Drive
San Diego, CA 92121

Dr. Michael Shore
Defense Nuclear Agency/SPSS
6801 Telegraph Road
Alexandria, VA 22310

Dr. Robert Shumway
University of California Davis
Division of Statistics
Davis, CA 95616

Dr. Matthew Sibol
Virginia Tech
Seismological Observatory
4044 Derring Hall
Blacksburg, VA 24061-0420

Prof. David G. Simpson
IRIS, Inc.
1616 North Fort Myer Drive
Suite 1050
Arlington, VA 22209

Donald L. Springer
Lawrence Livermore National Laboratory
L-025
P.O. Box 808
Livermore, CA 94550

Dr. Jeffrey Sievens
S-CUBED
A Division of Maxwell Laboratory
P.O. Box 1620
La Jolla, CA 92038-1620

Lt. Col. Jim Stobie
ATTN: AFOSR/NL
110 Duncan Avenue
Bolling AFB
Washington, DC 20332-0001

Prof. Brian Stump
Institute for the Study of Earth & Man
Geophysical Laboratory
Southern Methodist University
Dallas, TX 75275

Prof. Jeremiah Sullivan
University of Illinois at Urbana-Champaign
Department of Physics
1110 West Green Street
Urbana, IL 61801

Prof. L. Sykes
Lamont-Doherty Geological Observatory
 of Columbia University
Palisades, NY 10964

Dr. David Taylor
ENSCO, Inc.
445 Pineda Court
Melbourne, FL 32940

Dr. Steven R. Taylor
Los Alamos National Laboratory
P.O. Box 1663
Mail Stop C335
Los Alamos, NM 87545

Prof. Clifford Thurber
University of Wisconsin-Madison
Department of Geology & Geophysics
1215 West Dayton Street
Madison, WS 53706

Prof. M. Nafi Toksoz
Earth Resources Lab
Massachusetts Institute of Technology
42 Carleton Street
Cambridge, MA 02142

Dr. Larry Turnbull
CIA-OSWR/NED
Washington, DC 20505

Dr. Gregory van der Vink
IRIS, Inc.
1616 North Fort Myer Drive
Suite 1050
Arlington, VA 22209

Dr. Karl Veith
EG&G
5211 Auth Road
Suite 240
Suitland, MD 20746

Prof. Terry C. Wallace
Department of Geosciences
Building #77
University of Arizona
Tuscon, AZ 85721

Dr. Thomas Weaver
Los Alamos National Laboratory
P.O. Box 1663
Mail Stop C335
Los Alamos, NM 87545

Dr. William Wortman
Mission Research Corporation
8560 Cinderbed Road
Suite 700
Newington, VA 22122

Prof. Francis T. Wu
Department of Geological Sciences
State University of New York
 at Binghamton
Vestal, NY 13901

AFTAC/CA
(STINFO)
Patrick AFB, FL 32925-6001

DARPA/PM
3701 North Fairfax Drive
Arlington, VA 22203-1714

DARPA/RMO/RETRIEVAL
3701 North Fairfax Drive
Arlington, VA 22203-1714

DARPA/RMO/SECURITY OFFICE
3701 North Fairfax Drive
Arlington, VA 22203-1714

HQ DNA
ATTN: Technical Library
Washington, DC 20305

Defense Intelligence Agency
Directorate for Scientific & Technical Intelligence
ATTN: DTIB
Washington, DC 20340-6158

Defense Technical Information Center
Cameron Station
Alexandria, VA 22314 (2 Copies)

TACTEC
Battelle Memorial Institute
505 King Avenue
Columbus, OH 43201 (Final Report)

Phillips Laboratory
ATTN: XPG
29 Randolph Road
Hanscom AFB, MA 01731-3010

Phillips Laboratory
ATTN: GPE
29 Randolph Road
Hanscom AFB, MA 01731-3010

Phillips Laboratory
ATTN: TSML
5 Wright Street
Hanscom AFB, MA 01731-3004

Phillips Laboratory
ATTN: PL/SUL
3550 Aberdeen Ave SE
Kirtland, NM 87117-5776 (2 copies)

Dr. Michel Bouchon
I.R.I.G.M.-B.P. 68
38402 St. Martin D'Heres
Cedex, FRANCE

Dr. Michel Campillo   .
Observatoire de Grenoble
I.R.I.G.M.-B.P. 53
38041 Grenoble, FRANCE

Dr. Kin Yip Chun
Geophysics Division
Physics Department
University of Toronto
Ontario, CANADA

Prof. Hans-Peter Harjes
Institute for Geophysic
Ruhr University/Bochum
P.O. Box 102148   .
4630 Bochum 1, GERMANY

Prof. Eystein Husebye
NTNF/NORSAR
P.O. Box 51
N-2007 Kjeller, NORWAY

David Jepsen
Acting Head, Nuclear Monitoring Section
Bureau of Mineral Resources
Geology and Geophysics
G.P.O. Box 378, Canberra, AUSTRALIA

Ms. Eva Johannisson
Senior Research Officer
FOA
S-172 90 Sundbyberg, SWEDEN

Dr. Peter Marshall
Procurement Executive
Ministry of Defense
Blacknest, Brimpton
Reading FG7-FRS, UNITED KINGDOM

Dr. Bernard Massinon, Dr. Pierre Mechler
Societe Radiomana
27 rue Claude Bernard
75005 Paris, FRANCE (2 Copies)

Dr. Svein Mykkeltveit
NTNT/NORSAR
P.O. Box 51
N-2007 Kjeller, NORWAY (3 Copies)

Prof. Keith Priestley
University of Cambridge
Bullard Labs, Dept. of Earth Sciences
Madingley Rise, Madingley Road
Cambridge CB3 OEZ, ENGLAND

Dr. Jorg Schlittenhardt
Federal Institute for Geosciences & Nat'l Res.
Postfach 510153
D-3000 Hannover 51, GERMANY

Dr. Johannes Schweitzer
Institute of Geophysics
Ruhr University/Bochum
P.O. Box 1102148
4360 Bochum 1, GERMANY

Trust & Verify
VERTIC
8 John Adam Street
London WC2N 6EZ, ENGLAND

7